

The SPIRou Legacy Survey

Rotation period of quiet M dwarfs from circular polarization in near-infrared spectral lines: I. The SPIRou APERO analysis

P. Fouqué¹*, E. Martioli^{2,3}, J.-F. Donati¹, L.T. Lehmann¹, B. Zaire^{1,4}, S. Bellotti^{1,5}, E. Gaidos⁶, J. Morin⁷, C. Moutou¹, P. Petit¹, S.H.P. Alencar⁴, L. Arnold⁸, É. Artigau⁹, T.-Q. Cang¹⁰, A. Carmona¹¹, N.J. Cook⁹, P. Cortés-Zuleta¹², P.I. Cristofari¹, X. Delfosse¹¹, R. Doyon⁹, G. Hébrard³, L. Malo⁹, C. Reylié¹³, and C. Usher⁸

¹ Institut de Recherche en Astrophysique et Planétologie, Université de Toulouse, CNRS, 14 avenue Edouard Belin, F-31400, Toulouse, France, e-mail: Pascal.Fouque@irap.omp.eu

² Laboratório Nacional de Astrofísica, Rua Estados Unidos 154, 37504-364, Itajubá - MG, Brazil

³ Institut d’Astrophysique de Paris, CNRS, Sorbonne Université, 98 bis bd Arago, 75014 Paris, France

⁴ Departamento de Física-Icex-UFMG Antônio Carlos, 6627, 31270-901 Belo Horizonte, MG, Brazil

⁵ Science Division, Directorate of Science, European Space Research and Technology Centre (ESA/ESTEC), Keplerlaan 1, 2201 AZ, Noordwijk, The Netherlands

⁶ Department of Earth Sciences, University of Hawai’i at Mānoa, 1680 East-West Road, Honolulu, HI, 96822, USA

⁷ Laboratoire Univers et Particules de Montpellier, Université de Montpellier, CNRS, F-34095 Montpellier, France

⁸ Canada-France-Hawaii Telescope, CNRS, Kamuela, HI 96743, USA

⁹ Université de Montréal, Département de Physique, IREX, Montréal, QC H3C 3J7, Canada

¹⁰ Beijing Normal University, No.19, Xinjiekouwai St, Haidian District, Beijing, 100875, People’s Republic of China

¹¹ Université Grenoble Alpes, CNRS, IPAG, F-38000 Grenoble, France

¹² Laboratoire d’Astrophysique de Marseille, Aix-Marseille Université, CNRS, 38 rue Frédéric Joliot-Curie, F-13388, Marseille, France

¹³ Institut UTINAM, CNRS, Université Bourgogne Franche-Comté, OSU THETA Franche-Comté-Bourgogne, Observatoire de Besançon, BP 1615, 25010 Besançon Cedex, France

Received ; accepted

ABSTRACT

Context. The rotation period of stars is an important parameter along with mass, radius, effective temperature. It is an essential parameter for any radial velocity monitoring, as stellar activity can mimic the presence of a planet at the stellar rotation period. Several methods exist to measure it, including long sequences of photometric measurements or temporal series of stellar activity indicators.

Aims. Here, we use the circular polarization in near-infrared spectral lines for a sample of 43 quiet M dwarfs and compare the measured rotation periods to those obtained with other methods.

Methods. From Stokes V spectropolarimetric sequences observed with SPIRou at CFHT and the data processed with the APERO pipeline, we compute the least squares deconvolution profiles using different masks of atomic stellar lines with known Landé factor appropriate to the effective temperature of the star. We derive the longitudinal magnetic field to examine its possible variation along the 50 to 200 observations of each star. For determining the stellar rotation period, we apply a Gaussian process regression enabling us to determine the rotation period of stars with evolving longitudinal field.

Results. Among the 43 stars of our sample, we were able to measure a rotation period for 27 stars. For 8 stars, the rotation period was previously unknown. We find a good agreement of our rotation periods with periods found in the literature based on photometry and activity indicators and confirm that near-infrared spectropolarimetry is an important tool to measure rotation periods, even for magnetically quiet stars. Furthermore, we compute ages for 20 stars of our sample using gyrochronology.

Key words. stars: planetary systems – stars: individual – techniques: polarimetry, radial velocity

1. Introduction

Rotation period (hereafter P_{rot}) is an important characteristic of a star along with its effective temperature (T_{eff}), mass, radius and corresponding gravity ($\log g$), metallicity ($[M/H]$) and age. In the context of exoplanet search by velocimetry (measure of radial velocity RV), the knowledge of the stellar rotation period avoids attributing a periodogram peak to an exoplanet orbital period by taking into account the systematic noise introduced by stellar activity (e.g., Queloz et al. 2001). Several publications

* Based on observations obtained at the Canada-France-Hawaii Telescope (CFHT) which is operated from the summit of Maunakea by the National Research Council of Canada, the Institut National des Sciences de l’Univers of the Centre National de la Recherche Scientifique of France, and the University of Hawaii. Based on observations obtained with SPIRou, an international project led by Institut de Recherche en Astrophysique et Planétologie, Toulouse, France.

identified a periodic signal as due to activity and/or proposed methods to disentangle RV jitter from keplerian variation (see for example Bonfils et al. 2007; Figueira et al. 2010; Boisse et al. 2011) or identified a signal previously announced as due to a planet as actually being caused by activity (for instance Huélamo et al. 2008; Robertson et al. 2014; Robertson & Moshaver 2014; Kane et al. 2016; Faria et al. 2020).

Stellar rotation periods for magnetic stars have been measured using the small-scale surface magnetic field as evidenced by the broadening and intensification of some stellar lines due to the Zeeman effect (e.g., Babcock 1947) or the large-scale surface magnetic field derived from the polarimetric signal of spectral lines as pioneered by Preston (1971); Landstreet (1980) for early-type stars. A periodic variation of the longitudinal magnetic field is interpreted as due to the periodic appearance of magnetic regions at the surface of the star which allows one to measure its rotation period, see Landstreet (1992) for a review. An application to M dwarfs can be found in Donati et al. (2008); Morin et al. (2008, 2010); Hébrard et al. (2016).

Rotation periods can also be measured from long photometric sequences obtained with small telescopes such as ASAS (Pojmanski 1997), APT (Henry 1999), HATNet (Bakos et al. 2004), NSVS (Woźniak et al. 2004), SuperWASP (Pollacco et al. 2006), MEarth (Nutzman & Charbonneau 2008; Irwin et al. 2009): examples can be found among others in Kiraga & Stepien (2007); Irwin et al. (2011); Suárez Mascareño et al. (2016); Díez Alonso et al. (2019) or more recently from space telescopes such as Kepler, K2 or TESS (Díez Alonso et al. 2019).

An alternative technique uses sequences of stellar activity indicators such as $H\alpha$, Ca II H&K, Ca II infrared triplet (IRT), or values computed at the same time as the radial velocities using the cross-correlation function (CCF) such as full-width half-maximum (FWHM), contrast or bisector (e.g., Noyes et al. 1984; Queloz et al. 2001; Bonfils et al. 2007; West et al. 2008; Boisse et al. 2011; Bonfils et al. 2013; Suárez Mascareño et al. 2015; Nelson et al. 2016; Suárez Mascareño et al. 2018; Toledo-Padrón et al. 2019; Lafarga et al. 2021).

In the framework of the SPIRou Legacy survey (hereafter SLS), a sample of about 50 nearby low-mass stars is regularly monitored to detect exoplanets using the SPIRou spectropolarimeter (Donati et al. 2020). Some of these targets do not have a measured rotation period, and some have several measurements, sometimes in disagreement. To clarify the situation and increase the sample of known rotation periods, we focus in this paper on determining the rotation period by exploiting the large-scale magnetic field information extracted from Stokes V profiles of spectral lines.

The paper is organized as follows: Section 2 briefly describes SPIRou¹ and the SPIRou Legacy Survey (SLS²; id P40 and P42, PI: Jean-François Donati). Section 3 describes the generic software *A PipelinE to Reduce Observations* APERO³ v0.7.232, Cook et al. (2022) used to reduce the SPIRou observations, in particular the spectropolarimetric analysis and the derivation of the longitudinal magnetic field. Section 4 explains the results for the stars in our sample, separating them into 3 categories according to their spectral type. Two examples are treated in details, and comparison is made with results from the literature. Finally, Section 5 examines our general results and further perspectives.

¹ <http://spirou.irap.omp.eu> and <https://www.cfht.hawaii.edu/Instruments/SPIRou/>

² <http://spirou.irap.omp.eu/Observations/The-SPIRou-Legacy-Survey>

³ <https://github.com/njcu9999/apero-drs>

2. Observations

Observations are part of the CFHT large program SPIRou Legacy Survey. SPIRou is a stabilized high-resolution near-infrared (NIR) spectropolarimeter (Donati et al. 2020) mounted on the 3.6 m CFHT atop Maunakea, Hawaii. It is designed for high-precision velocimetry and spectropolarimetry to detect and characterize exoplanets and stellar magnetic fields. It provides a full coverage of the NIR spectrum from 950 nm to 2500 nm at a spectral resolving power of $\lambda/\Delta\lambda \sim 70\,000$.

The SLS was allocated 310 nights over 7 semesters (February 2019 to June 2022). It covers three different science topics, called work packages (see Donati et al. 2020 for details). The analysis of this paper is restricted to Work Package 1 (WP1), dedicated to blind planet search. More than 50 M dwarfs were regularly monitored during the SPIRou runs (typically 10 contiguous nights per month). We excluded from this study monitored active stars with short and well-known rotation periods ($P_{\text{rot}} < 5$ d): Gl 388 (AD Leo), Gl 406 (CN Leo), Gl 873 (EV Lac), Gl 1111 (DX Cnc), Gl 1154, Gl 1245B, Gl 3622, and PM J18482+0741. We, therefore, selected 43 stars in the original WP1 sample for which about 150 (min 50, max 250) polarimetric sequences (of 4 individual sub-exposures each) have been secured. This represents about 6800 visits corresponding to more than 27 000 individual spectra secured for the considered sample. Stars belonging to our sample and their stellar characteristics are given in Table 1: *Gaia* absolute magnitudes and colors use *Gaia* DR3 Gaia Collaboration et al. (2021); effective temperatures and metallicities come from Cristofari et al. (2022) who used the same set of observations and the same sample (except Gl 581 that does not satisfy our criterion of the minimum number of visits); masses are computed from absolute 2MASS K_s magnitude and metallicity using Mann et al. 2019 relations. The relative precision of these masses is 2-3% according to Mann et al. (2019), and internal errors amount to 30 K and 0.1 dex for T_{eff} and [M/H], respectively, according to Cristofari et al. (2022). We divide our sample into three sub-samples according to a proxy of stellar mass. These three mass bins correspond to the three types of magnetic behavior identified among active M dwarfs by Morin et al. (2010) (see Figure 15 therein). We prefer defining regions according to the absolute G magnitude rather than using the spectral types. Although they match on average, a low metallicity makes the star fainter at a given spectral type: Gl 412A (M1.0V, $[M/H] = -0.42$) is 1 mag fainter in G than Gl 410 (M1V, $[M/H] = +0.05$) so we feel that both should not belong to the same group. Horizontal lines in Table 1 separate the 3 sub-samples. The number of visits corresponds to the initial number, before rejection of some polarimetric sequences, for reasons explained in Sec. 3.2. Finally, we list the FWHM of the median Stokes I profile of each star because it is used to define the velocity range on which we measure the longitudinal magnetic field from the Stokes V profile, as explained in Sec. 3.2.

3. SPIRou data reduction and analysis

3.1. The APERO reduction

Our SPIRou data were reduced with the software APERO. APERO first performs some initial pre-processing of the 4096×4096 pixel images of the HAWAII 4RGTM (H4RG), applying a series of procedures to correct detector effects, remove background thermal noise, and identify bad pixels and cosmic ray impacts.

It then uses exposures of a quartz halogen lamp (flat) to calculate the position of 49 of the 50 échelle spectral orders

Table 1. Stellar characteristics of the sample of 43 M dwarfs. For uncertainties on mass, T_{eff} and [M/H], see text. The three sections correspond to early-, mid-, and late-type M dwarfs from top to bottom

Star Units	spectral type	M_G mag	$G_{\text{BP}} - G_{\text{RP}}$ mag	mass M_{\odot}	T_{eff} K	[M/H] dex	visits	FWHM Stokes I km s^{-1}
Gl 338B	M0V	8.046	1.846	0.58	3952	-0.08	58	6.95 ± 0.25
Gl 846	M0.5V	8.282	1.967	0.57	3833	0.07	194	6.65 ± 0.26
Gl 205	M1.5V	8.327	2.122	0.58	3771	0.43	160	6.54 ± 0.16
Gl 410	M1V	8.426	2.006	0.55	3842	0.05	131	7.73 ± 0.21
Gl 880	M1.5V	8.611	2.151	0.55	3702	0.26	166	6.37 ± 0.17
Gl 1514	M1.0V	8.793	2.088	0.50	3699	-0.07	177	5.84 ± 0.29
Gl 382	M2.0V	8.898	2.234	0.51	3644	0.15	124	6.34 ± 0.31
Gl 752A	M3.0V	9.240	2.379	0.47	3558	0.11	130	6.06 ± 0.23
Gl 48	M2.5V	9.364	2.459	0.46	3529	0.08	194	5.99 ± 0.26
Gl 617B	M3V	9.459	2.483	0.45	3525	0.20	149	6.09 ± 0.21
Gl 412A	M1.0V	9.460	2.104	0.39	3620	-0.42	224	5.50 ± 0.24
Gl 15A	M1.5V	9.460	2.164	0.39	3611	-0.33	256	5.76 ± 0.26
Gl 849	M3V	9.511	2.542	0.46	3502	0.35	203	6.17 ± 0.22
Gl 411	M2.0V	9.522	2.216	0.39	3589	-0.38	182	4.93 ± 0.18
Gl 480	M3.5V	9.565	2.591	0.45	3509	0.26	104	6.14 ± 0.22
Gl 436	M3.0V	9.631	2.449	0.42	3508	0.03	90	5.89 ± 0.33
Gl 687	M3.0V	9.739	2.518	0.39	3475	0.01	227	5.69 ± 0.20
Gl 408	M2.5V	9.831	2.430	0.38	3487	-0.09	179	6.17 ± 0.33
Gl 317	M3.5V	9.859	2.664	0.42	3421	0.23	79	5.39 ± 0.21
GJ 4063	M3.5V	9.982	2.770		3419	0.42	220	5.96 ± 0.22
Gl 725A	M3.0V	10.119	2.461	0.33	3470	-0.26	219	5.43 ± 0.22
Gl 251	M3.0V	10.129	2.561	0.35	3420	-0.01	187	5.73 ± 0.26
Gl 4333	M3.5V	10.233	2.818	0.37	3362	0.25	193	5.70 ± 0.16
GJ 1012	M4V	10.268	2.710	0.35	3363	0.07	142	5.26 ± 0.17
GJ 1148	M4V	10.370	2.778	0.34	3354	0.11	105	5.45 ± 0.16
Gl 876	M3.5V	10.527	2.809	0.33	3366	0.15	88	5.65 ± 0.28
PM J09553-2715	M3V	10.629	2.667	0.29	3366	-0.03	75	5.77 ± 0.25
PM J08402+3127	M3.5V	10.739	2.703	0.28	3347	-0.08	142	5.33 ± 0.25
Gl 725B	M3.5V	10.790	2.625	0.25	3379	-0.28	212	5.34 ± 0.22
GJ 1105	M4V	10.931	2.792	0.27	3324	-0.04	171	5.44 ± 0.17
Gl 445	M3.5V	10.948	2.702	0.24	3356	-0.24	94	5.21 ± 0.19
GJ 3378	M3.5V	10.975	2.791	0.26	3326	-0.05	177	5.65 ± 0.22
Gl 169.1A	M4V	10.994	2.896	0.28	3307	0.13	185	5.66 ± 0.28
GJ 1289	M3.5V	11.556	3.011	0.21	3238	0.05	209	7.60 ± 0.37
PM J21463+3813	M4V	11.591	2.814	0.18	3305	-0.38	187	5.21 ± 0.26
GJ 1103	M4.5V	11.817	3.116	0.19	3170	-0.03	70	5.44 ± 0.28
Gl 699	M4.0V	11.884	2.834	0.16	3311	-0.37	249	6.04 ± 0.32
Gl 15B	M3.5V	11.928	2.836	0.16	3272	-0.42	189	6.33 ± 0.37
Gl 447	M4.0V	11.960	3.033	0.18	3198	-0.13	60	6.24 ± 0.24
GJ 1151	M4.5V	12.158	3.142	0.17	3178	-0.16	157	6.42 ± 0.37
Gl 905	M5.5V	12.881	3.529	0.15	3069	0.05	220	6.13 ± 0.29
GJ 1286	M5.5V	13.344	3.706	0.12	2961	-0.23	113	7.46 ± 0.46
GJ 1002	M5.5V	13.347	3.675	0.12	2980	-0.33	146	6.92 ± 0.34

recorded on the detector. It optimally extracts (Horne 1986) spectra of the two science channels (fibers A and B) and the simultaneous reference channel (fiber C). This APERO extraction takes into account the non-Gaussian shape of the instrument profile generated by the pupil slicer. APERO corrects the spectra for the blaze signature of the echelle orders obtained from the flat-field exposures, as described in Cook et al. (2022). Both a 2-D order by order and 1-D order-merged spectrum are produced for each channel of each scientific exposure.

The pixel-to-wavelength calibration is obtained from exposures of both a Uranium-Neon hollow cathode lamp and a Fabry-Pérot etalon, generally following the procedure given in Hobson et al. (2021), but with differences described in Cook et al. (2022). Please refer to Sections 5.4 and 6.6 of the latter paper for details about the use of a reference night for the whole survey and updates for each survey night, with subtle differences in the wavelength calibration of fibers AB with respect to fibers A and B separately. This procedure provides wavelengths in the rest frame of the observatory, but APERO also

calculates the Barycentric Earth Radial Velocity (BERV) and the Barycentric Julian Date (BJD) of each exposure using the code `barycorpp`⁴ (Wright & Eastman 2014; Kanodia & Wright 2018). These can then be used to reference the wavelength and time to the barycentric frame of the solar system.

APERO calculates the spectrum of the telluric transmission using a novel technique based on a model obtained from the collection of standard star observations carried out since the beginning of SPIRou operations in 2019 and a fit made for each individual observation using a revised technique based on the principles explained in Artigau et al. (2014), as briefly described in Cook et al. (2022) and in more details in Artigau et al. (2022).

APERO also calculates the Stokes parameters describing the polarization state, as defined for instance in Landi Degl'Innocenti (1992). Each orthogonal polarization state is recorded on one science fiber. Four sub-exposures are taken with different positions of the quarter-wave rhombs: the method is described in Donati et al. (1997). The two polarization states of each sub-exposure are combined to define the Stokes parameters as explained in Sec. 10.1 of Cook et al. (2022) using equations defined in Bagnulo et al. (2009): the Stokes I parameter measures the intensity while the Stokes V parameter measures the circular polarization and the Stokes Q and U measure the linear polarization (not used in the present work). Another combination defines a null measurement to quantify the quality of the Stokes V detection. The continuum for Stokes I and V can be modeled by an iterative sigma-clip algorithm to fit a polynomial to the data. The spectra are normalized to this continuum before performing LSD analysis. More details are given in Martioli et al. (2020); Cook et al. (2022).

3.2. Spectropolarimetry analysis

We further analyze the SPIRou polarized spectra using the `spirou-polarimetry`⁵ code applied to the telluric-corrected 2D spectra. We assume that the APERO telluric correction is good enough so that we do not need to exclude zones of telluric water bands in this code. The Stokes I , Stokes V , and null polarization spectra are compressed to one line profiles using the least squares deconvolution (LSD) method of Donati et al. (1997). The line masks used in our LSD analysis were computed using the VALD3 catalog (Piskunov et al. 1995; Ryabchikova et al. 2015) and a MARCS model atmosphere (Gustafsson et al. 2008) with a grid of effective temperatures between 3000 K and 4000 K by steps of 500 K, a constant surface gravity of $\log g = 5.0$ dex and a micro-turbulent velocity v_{mic} of 1 km s^{-1} . We select all lines deeper than 3% and with a Landé factor of $g_{\text{eff}} > 0$, for a total of 2460, 1335 and 956 atomic lines for 4000 K, 3500 K and 3000 K, respectively. We normalize the Stokes V profile using a mean wavelength, a mean depth and a mean Landé factor of the lines in the mask, while using only the mean depth to normalize the Stokes I profile. For the 4000 K mask (respectively, 3500 K and 3000 K), the mean values are 1651.2 nm (respectively 1617.9 nm and 1604.8 nm) for the wavelengths, 0.135 (respectively 0.133 and 0.155) for the depths and 1.249 (respectively 1.242 and 1.235) for the Landé factors. To ensure that Stokes I LSD profiles have a continuum at 1, we use a linear regression of a significant number of bins located well outside of the line for each profile to improve the continuum normalization. We measure the standard deviation of the values in these bins and reject the profiles where this standard deviation signif-

icantly deviates from the average over all the profiles. This linear regression gives us a better defined Voigt profile, allowing a more precise measure of the FWHM of the median Stokes I LSD profile of each star.

Not all polarimetric sequences lead to a useful measurement of the longitudinal magnetic field. There are several steps of data rejection: the telluric correction of some spectra may fail, some LSD profiles are noisy enough that they cannot be fit by a Voigt profile, others can be fit but present a noisier continuum than the rest (see above) and are thus rejected. We have taken great care in rejecting data that could contaminate our results, especially to build a clean median Stokes I profile on which we measure the FWHM and define the velocity limits to integrate the Stokes V profile (using 6 FWHM as the measuring window, meaning ± 3 FWHM, generally about $\pm 20 \text{ km s}^{-1}$). The final number of polarimetric sequences used in our study is about 6500, compared to the 6800 initially available for our sample of stars, an acceptable loss of about 4% generally corresponding to low signal-to-noise ratio (SNR) spectra.

As an example, we take the LSD profiles of the early-M dwarf Gl 410 (DS Leo), which displays mild signs of magnetic activity. Fig. 1 shows the resulting LSD profiles at each observing epoch stacked vertically. Dynamical maps correspond from left to right to the intensity (Stokes I), the circular polarization (Stokes V), and the null LSD profiles. A non-zero Stokes V profile indicates the presence of magnetic fields, while the null profile allows us to assess the reliability of the Stokes V detection. Finally, Fig. 2 shows the median profile of our time series, where the Zeeman signature is clearly evidenced in the detection of the Stokes V profile. We also display a median null profile to assess the reliability of the detection of the Stokes V signature. For comparison, we display the Stokes I , V and null dynamical maps (Fig. 3) and median profiles (Fig. 4) of the late M dwarf Gl 905, whose longitudinal magnetic field has a similar amplitude to Gl 410. Here again, the Stokes V signal is clearly detected, with a shape corresponding at first order to the first derivative of the Stokes I profile.

In the Appendix, we display the Stokes V temporal evolution for each star of our sample. The Stokes I temporal evolution and the median Stokes profiles carry less important information for the present work, and the null profiles are very similar to each other, so for the sake of space, we decided not to publish them.

To check the consistency of our measurements, we also obtained an independent polarimetric reduction and LSD analysis of our SPIRou data using the Libre-Esprit pipeline (Donati et al. 1997, 2020). The results of this alternate analysis will be given in a forthcoming paper (Donati et al., in prep.).

3.3. Longitudinal magnetic fields

To diagnose the magnetic field in the present sample of stars we calculate the longitudinal magnetic field B_{ℓ} in the LSD profiles of SPIRou following the same prescription as in Rees & Semel (1979); Donati et al. (1997); Moutou et al. (2020); Martioli et al. (2020). B_{ℓ} is defined as the brightness-weighted line-of-sight-projected component of the vector magnetic field integrated over the visible hemisphere of the star, and is given in G by:

$$B_{\ell} = -2.142 \times 10^{11} \frac{\int v V(v) dv}{\lambda_0 \cdot g_{\text{eff}} \cdot c \cdot \int [1 - I(v)] dv}, \quad (1)$$

where c is the speed of light in the same unit as v (km s^{-1}), $I(v)$ is the Stokes I LSD profile normalized by the continuum and

⁴ <https://github.com/shbhuk/barycorpp>

⁵ <https://github.com/edermartioli/spirou-polarimetry>

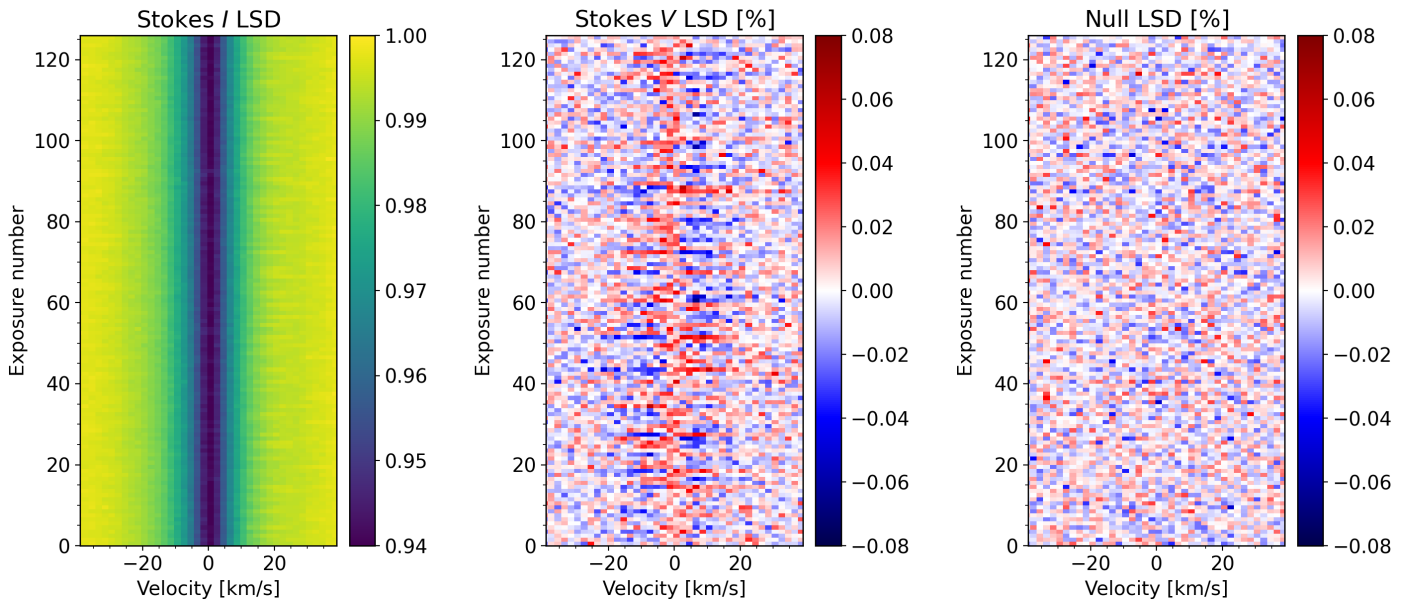


Fig. 1. Dynamical maps of Gl 410 constructed from individual observations (horizontal bands) stacked vertically. The first plot shows Stokes I LSD profiles, where the continuum is given in yellow and the different absorption depths are shown in green/blue shades. The following plots show respectively the Stokes V and null LSD profiles, where positive values are given as red shades and negative as blue shades. Note that Stokes V and null LSD amplitudes are expressed in per-cent. All plots are given in the rest frame of Gl 410 and display a velocity window of 10 FWHM (see Table 1).

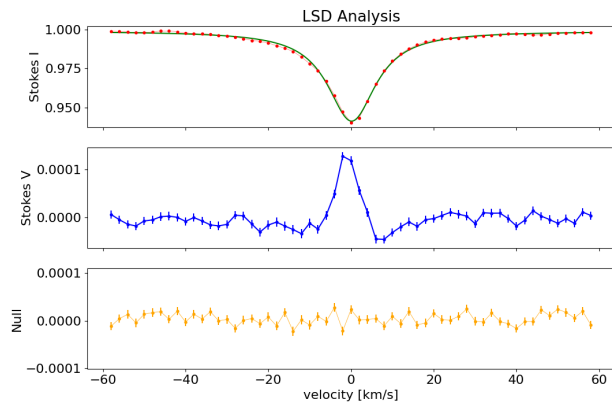


Fig. 2. Median of all LSD profiles in the Gl 410 SPIRou time series. The top panel shows Stokes I LSD (red points) with a Voigt profile model fit (green line); the middle panel shows Stokes V (blue points) and the bottom panel shows the null polarization profile (orange points).

$V(v)$ the Stokes V LSD profile, both as functions of the velocity v in the stellar frame, λ_0 is the mean wavelength in nm, and g_{eff} is the mean Landé factor of the lines included in the LSD analysis.

As the spatial distribution of the magnetic regions may be non axisymmetric, B_ℓ can be modulated by the star's rotation, allowing one to derive the stellar rotation period if any periodicity is detected in its time series (e.g., Preston 1971; Landstreet 1980). Examples focusing more on K and M dwarfs can be found in (e.g., Morin et al. 2008; Moutou et al. 2017; Petit et al. 2021). Fig. 5 and Fig. 6 show the generalized Lomb-Scargle (GLS) periodogram (Zechmeister & Kürster 2009) for the B_ℓ data calculated using the `astropy.timeseries`⁶ tool for our two example stars Gl 410 and Gl 905. We find a maximum power at

a period of 13.9 d for Gl 410, and at 108.6 d for Gl 905, both with a false alarm probability (FAP) below 0.001%. In the case of Gl 905, 3 other peaks below a FAP of 0.001% can be noticed in the periodogram, and they are due to harmonics of the main period.

As the magnetic field of M dwarfs is likely to evolve with time, this study requires a flexible model to account for the variability. We employ a Gaussian Process (GP) regression analysis (e.g., Haywood et al. 2014; Aigrain et al. 2015) using the code `george`⁷ (Ambikasaran et al. 2015), where we assume that the rotationally modulated stellar activity signal in B_ℓ is quasi-periodic (QP). Thus, we adopt a parameterized covariance function (or kernel) as in Angus et al. (2018), which is given by:

$$k(\tau_{ij}) = \alpha^2 \exp \left[-\frac{\tau_{ij}^2}{2l^2} - \frac{1}{\beta^2} \sin^2 \left(\frac{\pi \tau_{ij}}{P_{\text{rot}}} \right) \right] + \sigma^2 \delta_{ij}, \quad (2)$$

where $\tau_{ij} = t_i - t_j$ is the time difference between data points i and j , α^2 is the amplitude of the covariance, l is the decay time, β is the smoothing factor, P_{rot} is the star rotation period, and σ is an additional uncorrelated white noise, which adds a “jitter” term to the diagonal of the covariance matrix. This kernel combines a squared exponential component describing the overall covariance decay and a component that describes the periodic covariance structure, the amplitude of which is controlled by the smoothing factor⁸. Typical values of β vary between 0.25 and 1.25, the smaller values corresponding to multiple harmonics while the larger values emphasize single sinusoidal variation. Similarly, the decay parameter varies between a few tens to a few hundred days. As pointed out by Angus et al. (2018) the flexibility of this model can easily lead to an over-fitting of the data.

⁷ <http://dfm.io/george/current/>

⁸ Note that the definition of decay time scale and smoothing factor vary among researchers. The former is sometimes defined as $\sqrt{2}l$ (e.g., Petit et al. 2021), and $1/\beta^2$ may appear as Γ and be called harmonic complexity (e.g., Nicholson & Aigrain 2022).

⁶ <https://docs.astropy.org/en/stable/timeseries/lombscargle.html>

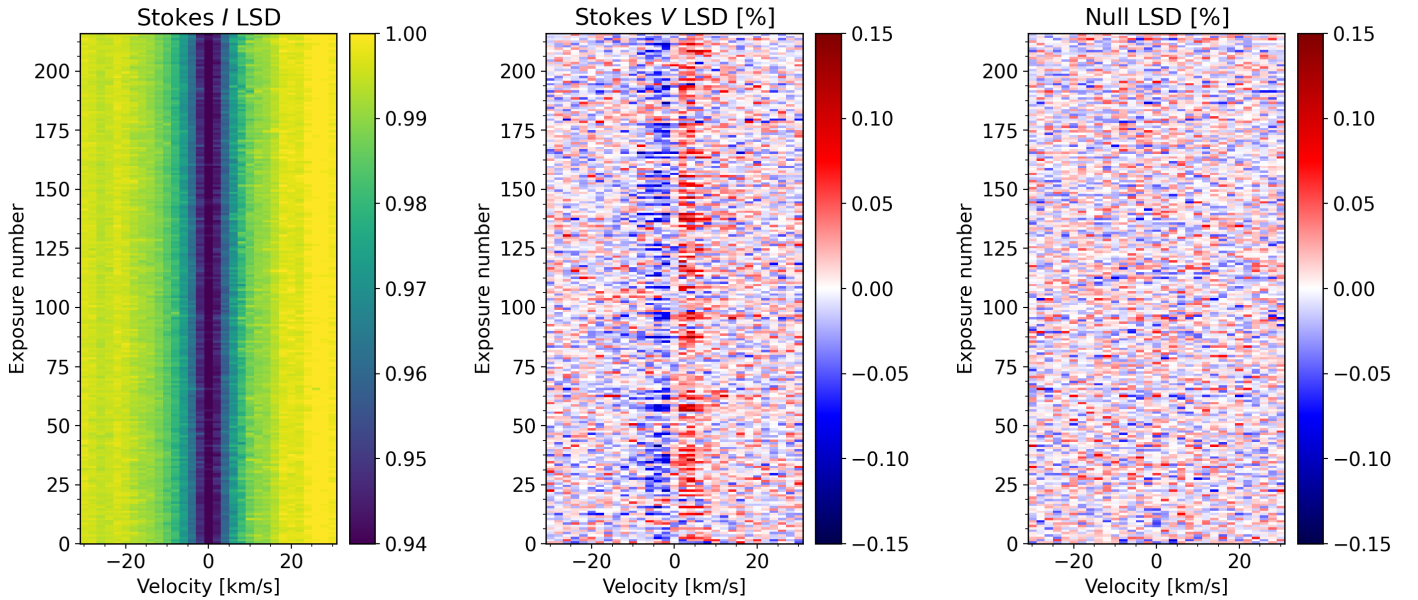


Fig. 3. Similar to Fig. 1, but for the dynamical maps of Stokes I , V and null LSD profiles collected for Gl 905 using SPIRou.

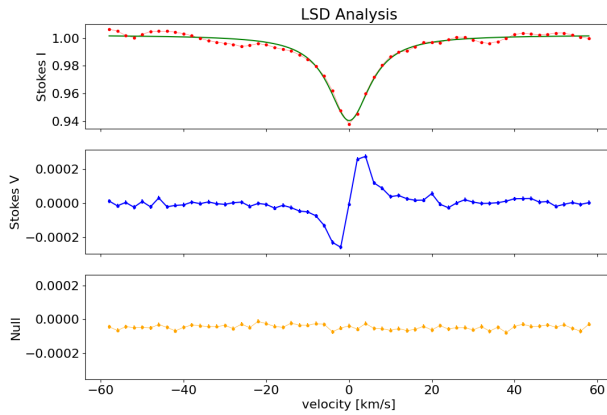


Fig. 4. Median of all LSD profiles in the Gl 905 SPIRou time series. The top panel shows Stokes I LSD (red points) with a Voigt profile model fit (green line); the middle panel shows Stokes V (blue points) and the bottom panel shows the null polarization profile (orange points).

To avoid this, we adopt a uniform prior distribution of the parameters (see Table 3 for instance) that restricts the search range to realistic values. In addition, when the posterior distribution of the smoothing factor and decay time does not display a clear peak, we restrict the fit from 6- to 5-parameter by fixing at 0.7 the value of the smoothing factor, which corresponds to the middle of the range of explored values and to the median value of stars with a constrained smoothing factor. We also explored a 4-parameter fit where both the smoothing factor and the decay time are fixed at 0.7 and 200 days, respectively, without finding significant differences with respect to the 5-parameter fit. The value of the fixed decay time is at best a guess and may depend on the spectral type (early-M stars seem to have a shorter decay time, around 70 days): Giles et al. (2017) using Kepler light curves find that "cooler stars have spots that last much longer, in particular for stars with longer rotational periods".

We use this GP framework to model the B_ℓ data, where we first fit the GP model parameters by the maximization of the like-

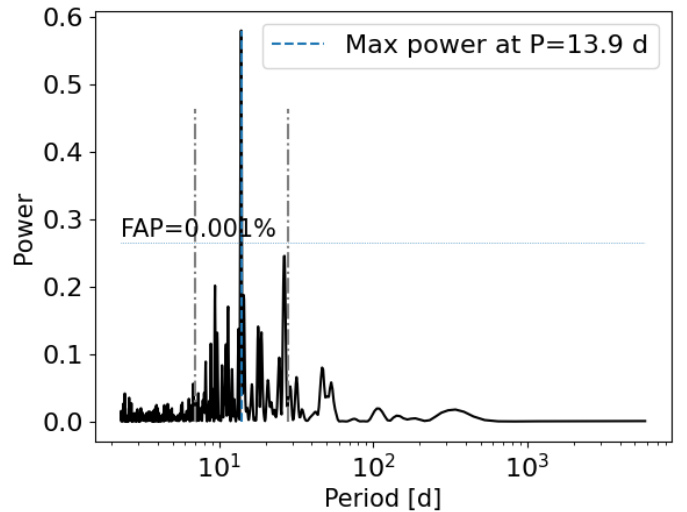


Fig. 5. Generalized Lomb-Scargle periodogram analysis of the longitudinal magnetic field (B_ℓ) time series of Gl 410. The blue dashed line shows the highest power at a period of 13.9 d, while the dot-dashed lines mark possible harmonics at half- and twice the period.

lihood function defined in Chapter 5 (Eq. 5.8)⁹ of Rasmussen & Williams (2006) and as implemented in `george`, and then we sample the posterior distribution of the free parameters using a Bayesian Markov chain Monte Carlo (MCMC) framework with the package `emcee` (Foreman-Mackey et al. 2013). We set the MCMC with 50 walkers, 1000 burn-in samples, and 5000 samples. The results of our analysis are illustrated in Fig. 7 and Fig. 9 where we present the observed B_ℓ data and the best-fit GP model for Gl 410 and Gl 905, respectively. Fig. 8 and Fig. 10 show the MCMC samples and posterior distributions of the GP parameters for a 6-parameter fit of the B_ℓ time series for Gl 410 and Gl 905, respectively.

⁹ <http://gaussianprocess.org/gpml/chapters/RW5.pdf>

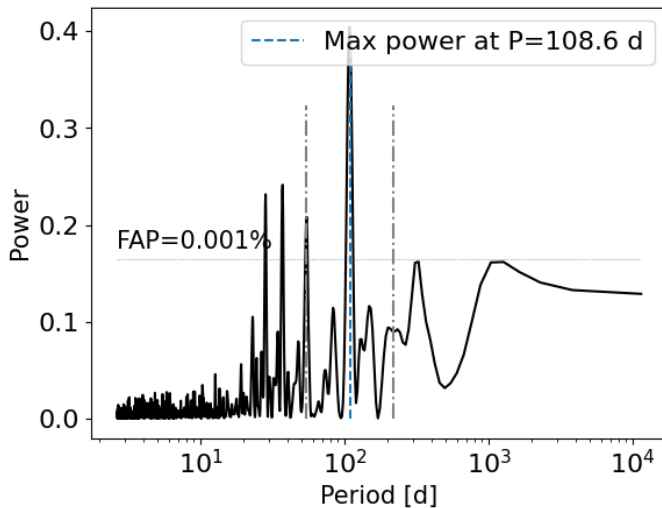


Fig. 6. GLS periodogram analysis of the longitudinal magnetic field (B_L) time series of Gl 905. The blue dashed line shows the highest power at a period of 108.6 d, while the dot-dashed lines mark possible harmonics at half- and twice the period.

4. Results

4.1. Early-type M dwarfs

Our sample includes 7 early-M dwarfs (M0V to M2V) with absolute magnitudes in the *Gaia* EDR3 G band between 8 and 9. With masses between 0.5–0.6 M_\odot they are partially convective. To compute the LSD profiles of these stars we use a mask with atomic lines of known Landé factor at 4000 K and $\log g=5.0$. For 6 of them, there is a clear variation of the longitudinal magnetic field and accordingly, the rotation period is measured quite accurately. We use the 6-parameter fit of the quasi-periodic GP model for them, but the decay time could not be well constrained for two of them. They are reported in Table 3, which gives the best-fit parameters measured as the median of the distribution with uncertainties given by the 0.16 and 0.84 quantiles. Here and in Tables 5 and 8, the number of visits corresponds to the final number after the rejection of bad polarimetric sequences, and therefore differs from the numbers listed in Table 1. Note that results for Gl 205 were already published in Cortes-Zuleta et al. (2023) based on a similar data set but on the *Libre-Esprit* data reduction and analysis package: the agreement of the measured parameters is encouraging, see Table 2. Rotation periods lie between 11 and 38 d for this sample. As the radius of early-type M dwarfs is in the range 0.5–0.6 R_\odot , such rotation periods translate into equatorial velocities below 3 km s^{-1} . This $v \sin i$ is below the detectability threshold of our spectrograph ($2\text{--}3 \text{ km s}^{-1}$). A broadening of the FWHM of the Stokes I profile may be due to several factors when the rotation is negligible: for active stars, it may come from a Zeeman broadening effect, but for quiet stars studied in this sample it is probably due to other factors. In Sec. 5, we return to this topic once we have the full sample analyzed. For the earliest spectral-type star Gl 338B, the Stokes V signal is clearly detected, see Fig. C.1. However, we failed to detect any periodicity in the longitudinal magnetic field variation, probably due to the low number of visits (58 observations).

Looking at the GP parameters, it appears that the decay time is pretty well constrained with values clustering around 75 d. The smoothing parameter varies more widely, between 0.5 (several harmonics) and 1.0 (smooth variation). For two stars where the smoothing parameter and the decay time are not well con-

strained, we used a 5-parameter fit by fixing the smoothing parameter to 0.7. The white noise is always compatible with 0 within 2σ , meaning that the GP does not need an additional variable to explain the dispersion, and the reduced χ^2 are close to 1. It is noticeable that we reach an rms of the fit of a few G for these stars. The results are summarized in Table 3.

Rotation periods were already known for all these stars, based on a variety of indicators: ZDI analysis, photometry (noted "phm" in Tables 4, 6, 9), and activity indicators (noted "act" in the same Tables). In Table 4 we compare our new values to those from the literature. There is generally a good agreement, but some literature values are discrepant for unclear reasons (see for instance Gl 846) or reveal a harmonic (twice the frequency of rotation: Gl 382 for Sabotta et al. (2021)). Photometry and activity measurements may be affected by sporadic variability (flares), and poor sampling may lead to differences or detection of harmonics of the true rotation period. A case by case discussion is difficult as the literature values are based on different techniques with varying precision, time sampling and total time coverage. For our method, the time sampling and total coverage are generally adequate and the precision is quite uniform after rejecting low SNR measurements.

4.2. Mid-type M dwarfs

This is the most numerous sub-category in our sample, comprising 26 stars with M_G between 9 and 11, spectral types ranging from M1V to M4V, and masses between 0.2 and 0.5 M_\odot . This group crosses the so-called "Jao gap" (Jao et al. 2018) at about $M_G=10.2$, $G_{\text{BP}}-G_{\text{RP}}=2.3$ and includes the transition between partially convective and fully convective M dwarfs. As the transition mass between these two regimes is not well defined (0.2 to 0.35 M_\odot) and depends on metallicity (see Feiden et al. 2021 for a more detailed discussion), we prefer not to try to define a finer grid of magnitudes or spectral types with the risk of a possibly inhomogeneous sub-category. To compute the LSD profiles of these stars we use a mask with atomic lines of known Landé factor at 3500 K and $\log g=5.0$.

In contrast with the group of early-M dwarfs, here only half of the stars evidences a detection of their rotation period. We first try a 6-parameter fit of the quasi-periodic GP model for them, but only three stars have a well constrained decay time at about 100 days. For the other stars where we could determine a rotation period, we use a 5- or even a 4-parameter fit, fixing the smoothing parameter at 0.7 (5-parameter fit) and when necessary the decay time to 200 days (4-parameter fit). Among the stars in this group, we detect a very long periodic variation of about 450 days for Gl 411 in clear disagreement with the shorter period reported from photometry by Díaz et al. (2019) of 56.15 ± 0.27 d, and unexpectedly long compared to all the M dwarfs with known stellar rotation periods (see Fig. 11. It would imply an unknown mechanism of angular momentum loss. We show in Appendix B the GP fit in Fig. B.1 corresponding to this particular star and its associated corner plot in Fig. B.3. The measured period may in fact correspond to a cyclic variation of the magnetic field more related to the variation of the activity than to the stellar rotation.

We were able to measure the rotation period for half of the mid-M dwarfs compared to 100% for the early-M dwarfs. Furthermore, a 6-parameter fit could only be measured for 3 stars compared to 4 out of 6 for the early-M dwarfs. This may come from a longer decay time not being constrained enough by our 3-yr survey. The shape of the variation of the longitudinal magnetic field varies a lot, from almost sinusoidal variations for Gl 169.1A (smoothing factor of 1) to a variation featuring only a few har-

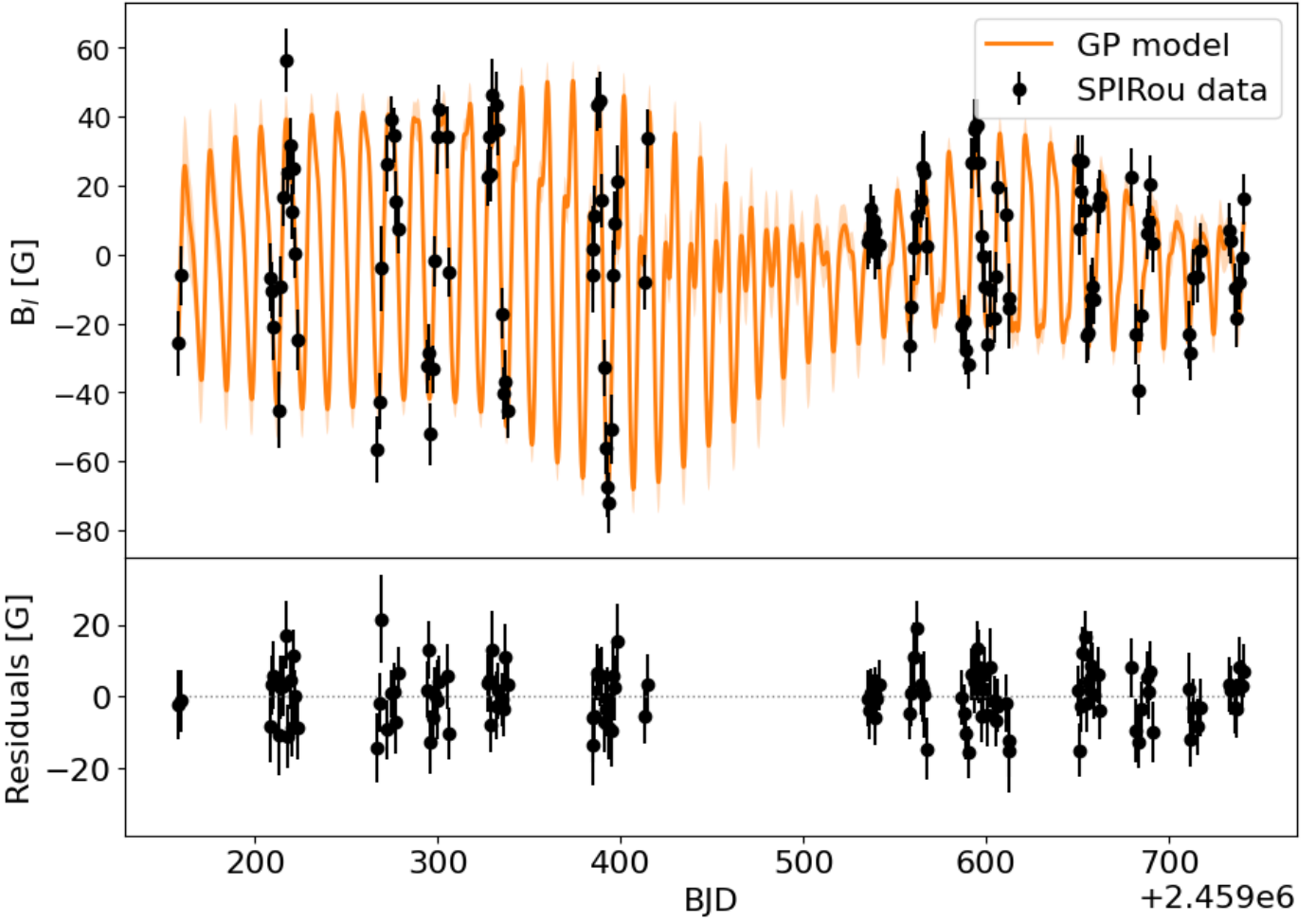


Fig. 7. GP analysis of the SPIRou B_ℓ data of Gl410. In the top panel, the black points show the observed B_ℓ data and the orange line shows the best-fit quasi-periodic GP model. Bottom panel shows the residuals with an RMS dispersion of 7.6 G.

Table 2. Best 6-parameter fit of a quasi-periodic GP model obtained in our analysis of the stellar activity from the SPIRou B_ℓ data of Gl205, compared to the results from Cortes-Zuleta et al. (2023) using a similar data set but the Libre-Esprit data reduction and analysis package.

Package	rotation period P_{rot} [d]	mean B_ℓ μ [G]	white noise σ [G]	amplitude α [G]	decay time l [d]	smoothing factor β	rms [G]	χ^2_{red}	visits
APERO	$34.3^{+0.4}_{-0.4}$	$2.5^{+2.0}_{-2.0}$	$1.0^{+0.5}_{-0.6}$	$7.1^{+1.3}_{-1.0}$	67^{+15}_{-11}	$0.54^{+0.09}_{-0.07}$	2.5	0.79	152
Libre-Esprit	$34.4^{+0.5}_{-0.4}$	$1.3^{+0.9}_{-0.9}$	$0.4^{+0.2}_{-0.2}$	$3.1^{+0.6}_{-0.4}$	63^{+13}_{-8}	$0.57^{+0.10}_{-0.08}$	0.94	0.84	153

Table 3. Best 6-parameter fit of a quasi-periodic GP model obtained in our analysis of the stellar activity from the SPIRou B_ℓ data of the early-type M dwarfs in our sample.

Star	rotation period P_{rot} [d]	mean B_ℓ μ [G]	white noise σ [G]	amplitude α [G]	decay time l [d]	smoothing factor β	rms [G]	χ^2_{red}	visits
Priors	$\mathcal{U}(2, 300)$	$\mathcal{U}(-\infty, +\infty)$	$\mathcal{U}(0, +\infty)$	$\mathcal{U}(0, +\infty)$	$\mathcal{U}(50, 1000)$	$\mathcal{U}(0.25, 1.25)$			
Gl846	$11.01^{+0.17}_{-0.22}$	$-0.6^{+2.0}_{-2.1}$	$2.6^{+1.0}_{-1.3}$	$6.2^{+1.4}_{-1.2}$	57^{+18}_{-5}	$0.96^{+0.19}_{-0.22}$	6.1	1.05	188
Gl205	$34.3^{+0.4}_{-0.4}$	$2.5^{+2.0}_{-2.0}$	$1.0^{+0.5}_{-0.6}$	$7.1^{+1.3}_{-1.0}$	67^{+15}_{-11}	$0.54^{+0.09}_{-0.07}$	2.5	0.79	152
Gl410	$13.87^{+0.08}_{-0.07}$	$-1.1^{+10.8}_{-10.5}$	$3.7^{+2.0}_{-2.2}$	$28.9^{+6.7}_{-4.7}$	78^{+16}_{-14}	$0.73^{+0.13}_{-0.10}$	7.6	0.86	126
Gl880	$37.7^{+0.8}_{-0.6}$	$4.0^{+3.4}_{-3.1}$	$0.8^{+0.8}_{-0.6}$	$11.4^{+2.4}_{-1.7}$	94^{+24}_{-20}	$0.56^{+0.10}_{-0.08}$	3.8	0.65	162
Gl514	$30.45^{+0.13}_{-0.14}$	$-4.2^{+5.9}_{-5.4}$	$2.1^{+1.3}_{-1.4}$	$8.8^{+3.6}_{-2.4}$		$0.99^{+0.18}_{-0.25}$	8.2	1.10	165
Gl382	$21.32^{+0.04}_{-0.03}$	$-0.7^{+4.2}_{-4.2}$	$2.8^{+1.2}_{-1.5}$	$7.9^{+3.2}_{-1.9}$		$0.62^{+0.27}_{-0.18}$	6.7	1.11	114

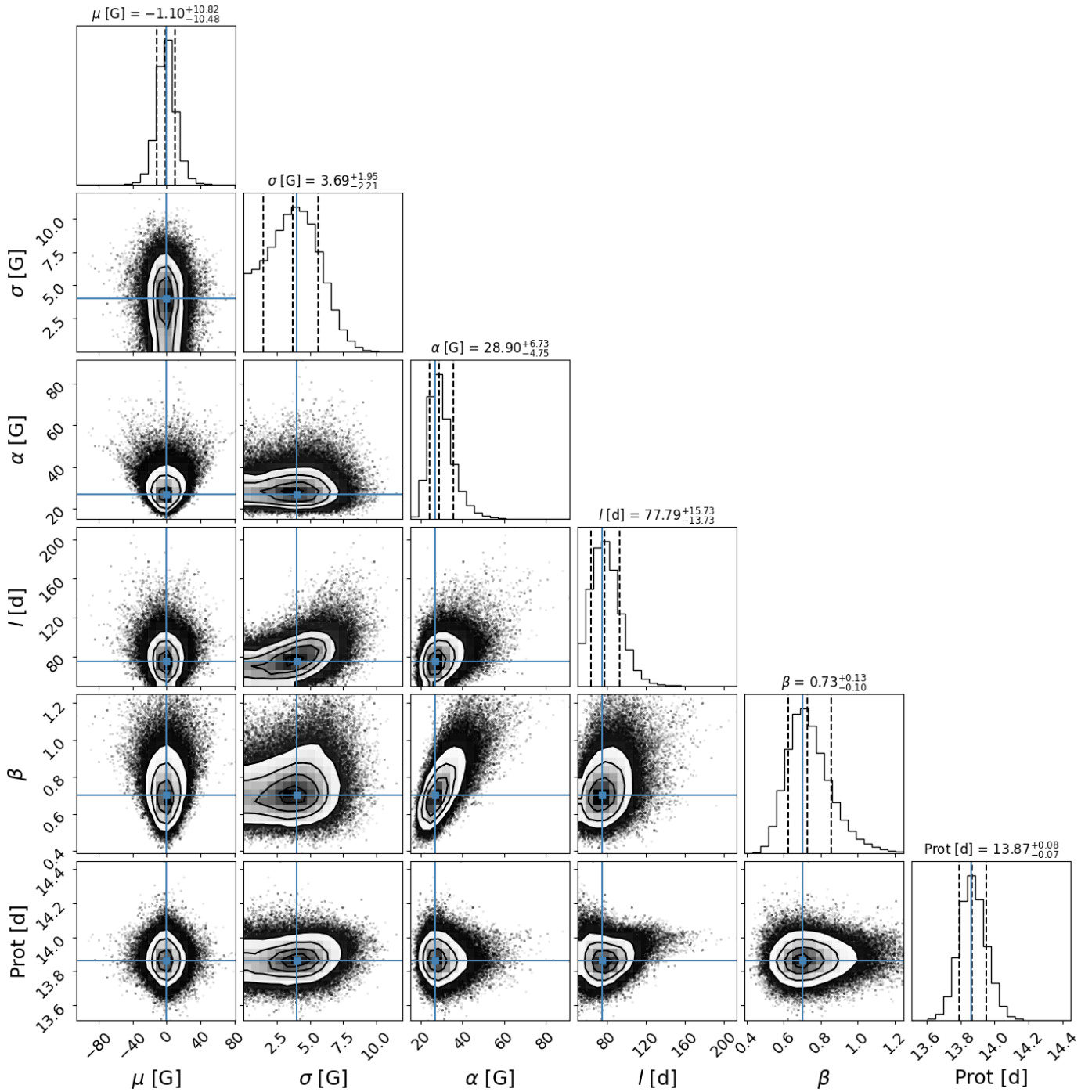


Fig. 8. MCMC samples and the posterior distributions of parameters in the quasi-periodic GP analysis of the stellar activity in the SPIRou B_ℓ data of Gl 410. The blue crosses mark the mode of the distribution, while the vertical dashed lines in the histograms mark the median and the 16 and 84 percentiles of the posterior probability density function (PDF). The shaded regions correspond to uncertainties of 1, 2, 3 σ in order of increasing radius.

monics for Gl 48, GJ 3378 or GJ 4333 (smoothing factor of 0.6). The amplitude of the variations ranges from very weak (5 G for Gl 411) to about 20 G for GJ 4333 and Gl 876. For this group, the white noise component of the GP is always compatible with 0 at 2σ , as it was the case for the early-M dwarfs.

In Table 6 we compare our new values of rotation period to those from the literature. There is generally a good agreement, but some literature values are discrepant. Excluding possible sampling problems or low number of measurements in one case (Gl 876), there may be more fundamental reasons for some

techniques to succeed or fail on a given star: photometric variations may be affected by flares while longitudinal magnetic field of the star may stay constant due to an axisymmetric field topology that prevents us from detecting a periodic variation even when Stokes V profiles show a clear detection. At least in one case, Gl 411, the very long measured period may in fact reflect a cyclic variation of activity rather than the stellar rotation period. We will also see at the end of Sec. 4.3 that some stars have a clear detection of the Stokes V profile but no rotation period detected when the magnetic field is axisymmetric.

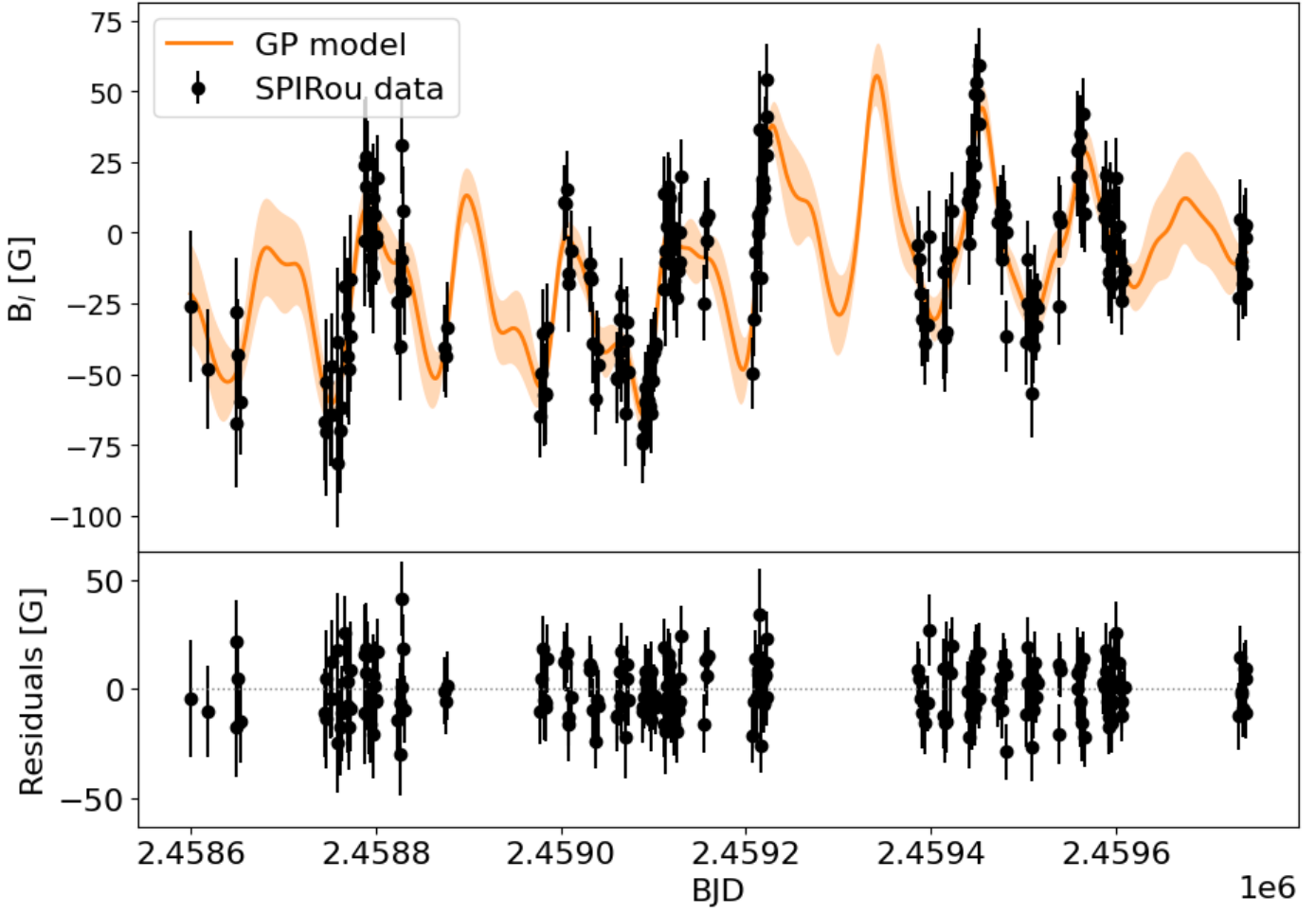


Fig. 9. GP analysis of the SPIRou B_ℓ data of Gl 905. In the top panel the black points show the observed B_ℓ data and the orange line shows the 6-parameter best-fit quasi-periodic GP model. Bottom panel shows the residuals with an RMS dispersion of 13 G.

Table 4. Comparison of the rotation periods given in the literature with our measured values for the early-M stars.

Reference	Category	Gl 205	Gl 382	Gl 410	Gl 514	Gl 846	Gl 880
This work	B_ℓ	34.3 ± 0.4	21.32 ± 0.04	13.87 ± 0.08	30.45 ± 0.14	11.01 ± 0.20	37.7 ± 0.7
Kiraga & Stepień (2007)	phm	33.61	21.56				
Donati et al. (2008)	ZDI			14.0			
Bonfils et al. (2013)	act	32.8, 39.3					10.7
Suárez Mascareño et al. (2015)	act	35.0 ± 0.1	21.7 ± 0.1		28.0 ± 2.9	31.0 ± 0.1	37.5 ± 0.1
Suárez Mascareño et al. (2016)	phm	33.4 ± 0.1	21.2 ± 0.1				
Hébrard et al. (2016)	ZDI	33.63 ± 0.37		13.83 ± 0.10		10.73 ± 0.10	
Suárez Mascareño et al. (2017)	act	34.8 ± 1.3	21.8 ± 0.1		30.0 ± 0.9	26.3 ± 5.6	37.2 ± 6.7
Díez Alonso et al. (2019)	phm	33.8 ± 0.6	21.6 ± 0.2	14.6 ± 0.2		29.5 ± 0.1	39.5 ± 0.2
Sabotta et al. (2021)	act	37.08	10.65, 21.4				

We also tested the results of the Libre-Esprit pipeline as given in Carmona et al. (in prep) for Gl 388 (AD Leo) even if this star was discarded from our sample for being too active. Table 7 compares the results, which are in excellent agreement.

4.3. Late-M dwarfs

The last group contains 10 stars with M_G above 11 (up to 13.5), spectral types from M3.5V to M5.5V, and masses between 0.1 and 0.2 M_\odot . These stars are fully convective. Later spectral type

stars (M6.0V, M6.5V) in the WP1 sample are all active stars with short rotation periods and are therefore excluded from the present study. To compute the LSD profiles of these late-type stars we use a mask with atomic lines of known Landé factor at 3000 K and $\log g=5.0$. We generally have to use a 4-parameter fit of the quasi-periodic GP model for them, fixing the smoothing parameter to 0.7 and the decay time to 200 days, except for two stars in this group for which a 6-parameter fit gives well-constrained values of the smoothing factor and the decay time. The others are marked with an asterisk in Table 8. For only one star, Gl 447 (Ross 128, F1 Vir), we could not confirm the long ro-

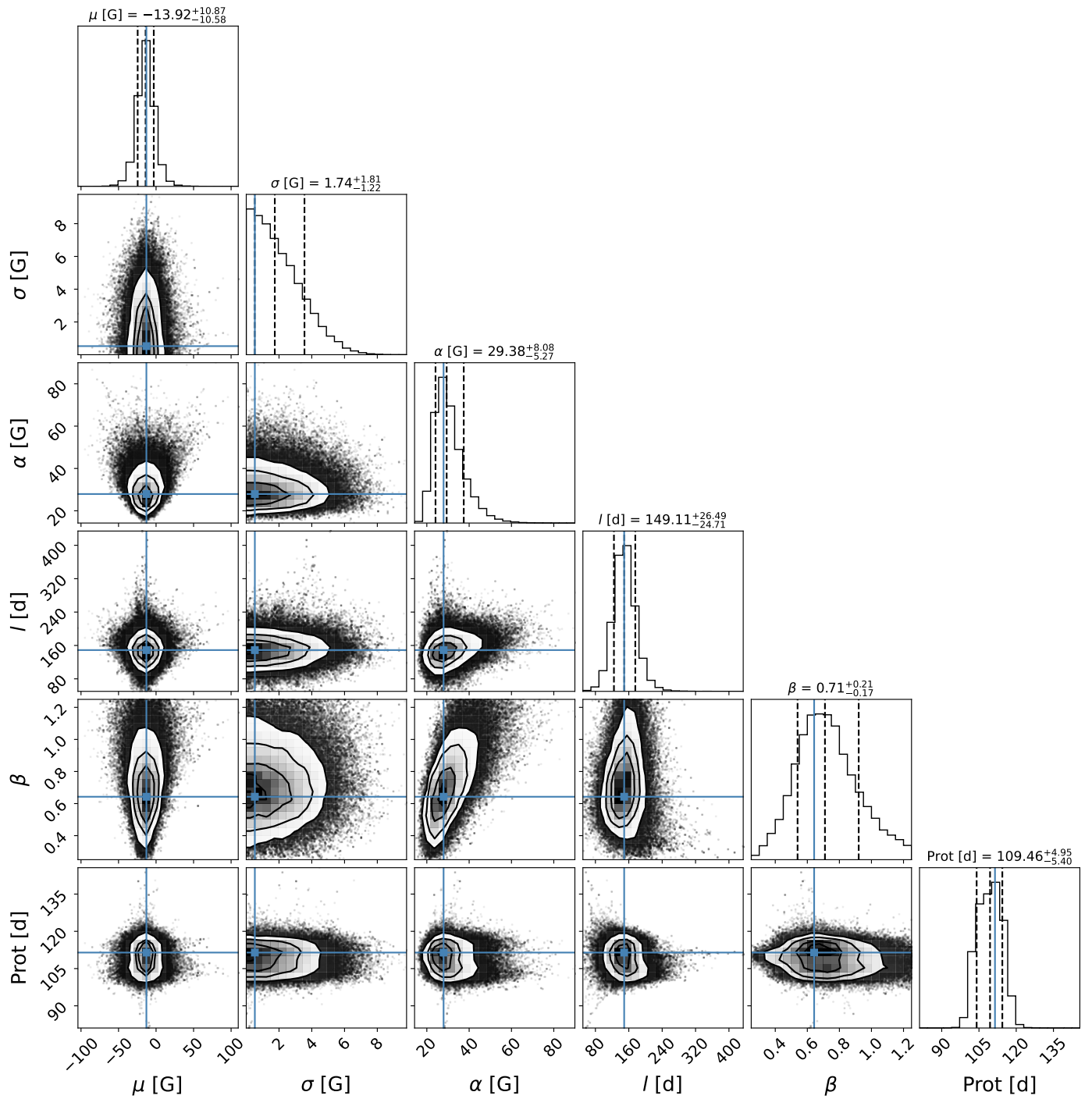


Fig. 10. MCMC samples and the posterior distributions of the 6-parameter fit of a quasi-periodic GP on the SPIRou B_ℓ data of Gl 905. The same format as in Fig. 8 is used.

tation period measured from ASAS photometry by Suárez Martínez et al. (2016) (165.1 ± 0.8 d) and Díez Alonso et al. (2019) (163 ± 3 d). This is probably due to the low number and distribution of the visits (57 clustered into two groups) compared to the other late-M dwarfs, which prevents us from determining Gl 447's rotation period. It highlights once again that our set limit to 50 visits with adequate sampling is essential. Below this value, the determination of the rotation period becomes difficult.

In Table 9 we compare our new rotation periods to those from the literature. The agreement is not as good as for earlier M dwarfs, probably due to their longer periods of rotation

and larger uncertainties. It becomes naturally harder to determine very long periods as we are limited by the time range of the SPIRou observations.

Finally, in Table 10 we present the data of the 16 stars for which we could not measure a rotation period. For these stars, we arbitrarily fixed the decay parameter to 200 d and the smoothing factor to 0.7 to get some indications about the mean B_ℓ , residual white noise, and amplitude of the field. The GP also gives a value of the rotation period but we do not list it as it is not well constrained. We assume that the values of the other parameters of the GP still bear some information, although the fact that the

Table 5. Best 6- to 4-parameter fit of a quasi-periodic GP model obtained in our analysis of the stellar activity from the SPIRou B_ℓ data of the mid-range M dwarfs in our sample. The asterisk after a star name means that the measured period is more uncertain and has been obtained by a 5- or 4-parameter fit only.

Star	rotation period P_{rot} [d]	mean B_ℓ μ [G]	white noise σ [G]	amplitude α [G]	decay time l [d]	smoothing factor β	rms [G]	χ^2_{red}	visits
Priors	$\mathcal{U}(2, 300)$	$\mathcal{U}(-\infty, +\infty)$	$\mathcal{U}(0, +\infty)$	$\mathcal{U}(0, +\infty)$	$\mathcal{U}(50, 1000)$	$\mathcal{U}(0.25, 1.25)$			
Gl 752A	$53.2^{+5.5}_{-3.0}$	$0.2^{+3.4}_{-3.2}$	$1.6^{+1.3}_{-1.1}$	$8.6^{+2.9}_{-1.9}$	93^{+55}_{-29}	$0.89^{+0.24}_{-0.29}$	6.2	0.87	128
Gl 48	$51.2^{+1.4}_{-1.4}$	$-7.0^{+3.6}_{-3.7}$	$1.8^{+1.6}_{-1.2}$	$10.2^{+3.2}_{-2.1}$	112^{+55}_{-36}	$0.62^{+0.22}_{-0.16}$	9.4	0.86	188
Gl 15A	$44.3^{+2.0}_{-2.0}$	$-1.0^{+1.8}_{-1.7}$	$1.0^{+0.9}_{-0.7}$	$5.4^{+1.4}_{-1.0}$	85^{+36}_{-22}	$0.71^{+0.28}_{-0.23}$	5.6	0.82	246
Gl 849	$41.4^{+0.4}_{-0.4}$	$4.7^{+6.3}_{-5.9}$	$2.4^{+1.6}_{-1.6}$	$12.1^{+5.1}_{-3.2}$		$0.87^{+0.24}_{-0.23}$	10.0	1.01	185
Gl 411	471^{+41}_{-40}	$5.9^{+2.4}_{-2.1}$	$0.8^{+0.8}_{-0.6}$	$4.2^{+1.8}_{-1.1}$		$0.68^{+0.32}_{-0.27}$	6.3	0.94	212
Gl 687	$56.5^{+1.3}_{-0.5}$	$4.9^{+8.9}_{-6.4}$	$1.7^{+1.3}_{-1.1}$	$13.3^{+7.3}_{-4.3}$		$0.97^{+0.19}_{-0.26}$	8.2	1.10	214
Gl 725A	$103.5^{+4.6}_{-5.1}$	$-14.9^{+3.4}_{-3.1}$	$1.2^{+1.2}_{-0.8}$	$8.7^{+2.4}_{-1.6}$			8.1	0.81	214
Gl 251*	$98.7^{+11.5}_{-4.8}$	$17.4^{+3.6}_{-3.6}$	$1.7^{+1.6}_{-1.2}$	$8.3^{+2.4}_{-1.9}$			9.9	0.85	177
GJ 4333*	$72.0^{+0.9}_{-1.2}$	$6.8^{+8.9}_{-8.0}$	$2.6^{+2.1}_{-1.7}$	$18.5^{+8.9}_{-4.1}$		$0.55^{+0.25}_{-0.17}$	12.7	0.83	190
Gl 876	$82.8^{+2.0}_{-0.7}$	$3.5^{+13.3}_{-13.5}$	$2.0^{+1.9}_{-1.4}$	$23.0^{+12.3}_{-7.1}$		$0.72^{+0.24}_{-0.19}$	8.5	0.92	88
PM J09553-2715*	$70.5^{+5.7}_{-1.9}$	$15.4^{+9.8}_{-11.7}$	$2.7^{+2.4}_{-1.9}$	$15.1^{+8.7}_{-5.1}$		$0.82^{+0.30}_{-0.33}$	11.8	0.91	74
GJ 3378*	$92.1^{+4.1}_{-5.3}$	$13.6^{+5.6}_{-5.4}$	$4.6^{+2.3}_{-2.7}$	$12.0^{+5.1}_{-2.8}$		$0.61^{+0.32}_{-0.23}$	13.9	1.00	174
Gl 169.1A	$91.9^{+4.1}_{-2.6}$	$2.3^{+8.4}_{-7.2}$	$1.9^{+1.9}_{-1.3}$	$11.4^{+5.3}_{-3.3}$		$1.04^{+0.15}_{-0.23}$	13.4	0.91	172

Table 6. Comparison of the rotation periods given in the literature with our measured values for the mid-M stars.

Reference	Category	Gl 752A	Gl 48	Gl 15A	Gl 849	Gl 411	Gl 687	Gl 251	GJ 4333	Gl 876	GJ 3378
This work	B_ℓ	53 ± 4	51.2 ± 1.4	44.3 ± 2.0	41.4 ± 0.4	470 ± 40	56.5 ± 0.9	99 ± 8	72.0 ± 1.0	82.8 ± 1.4	92 ± 5
Rivera et al. (2005)	phm									96.7 ± 1.0	
Bonfils et al. (2013)	act									$61.0, 30.1$	
Burt et al. (2014)	phm					$2000 ?$					
Howard et al. (2014)	phm							61.8 ± 1.0			
Suárez Mascareño et al. (2015)	act	46.5 ± 0.3								87.3 ± 5.7	
Nelson et al. (2016)	act									95 ± 1	
Suárez Mascareño et al. (2016)	phm	46.0 ± 0.2									
Moutou et al. (2017)	ZDI								90 ± 10		
Suárez Mascareño et al. (2017)	act									90.9 ± 16.5	
Suárez Mascareño et al. (2018)	act										
Díaz et al. (2019)	phm				45.0 ± 4.4						
Díez Alonso et al. (2019)	phm	46.0 ± 0.2	51.5 ± 2.6				56.15 ± 0.27				
Reinhold & Hekker (2020)	phm								18.1 ± 0.3	74.7 ± 0.7	81.0 ± 0.8
Stock et al. (2020)	phm										31.31 ± 8.15
Sabotta et al. (2021)	act	174.48	43.39						122.1 ± 2.2		
									67.59, 119.48		83.39

Table 7. Best 6-parameter fit of a quasi-periodic GP model obtained in our analysis of the stellar activity from the SPIRou B_ℓ data of Gl 388 (AD Leo), compared to the results from Carmona et al. (in prep) using a similar data set but the Libre-Esprit data reduction and analysis package.

Package	rotation period P_{rot} [d]	mean B_ℓ μ [G]	white noise σ [G]	amplitude α [G]	decay time l [d]	smoothing factor β	rms [G]	χ^2_{red}	visits
APERO	$2.2301^{+0.0019}_{-0.0017}$	-156^{+43}_{-42}	$4.6^{+3.3}_{-3.0}$	68^{+21}_{-14}	220^{+41}_{-40}	$1.35^{+0.11}_{-0.19}$	12.7	0.91	70
Libre-Esprit	$2.2304^{+0.0015}_{-0.0013}$	-156^{+47}_{-44}	$5.4^{+3.7}_{-3.6}$	67^{+23}_{-15}	255^{+96}_{-77}	$1.36^{+0.10}_{-0.17}$	14.7	0.96	69

rotation period is not constrained and that 2 parameters of the GP are arbitrarily fixed limit the value of this information. For completeness, we list a period and its reference, when available in the literature, but this information was not used in our GP fit.

Looking at the Stokes V profiles in Appendix C, we may tentatively explain these non-detections by their magnetic topology: if the magnetic field is axisymmetric, we cannot detect the rotation modulation. To test this interpretation, we measured the

rate of detection of Stokes V profiles for a given star by comparison to the noise measured in a velocity region well outside of the line. We find that this metric quantifies quite well the visual impression of the time series of Stokes V profiles as shown in Appendix C. Then, we subtract a median Stokes V profile for each star and measure again the detection rate. For some stars it changes dramatically, and we tentatively interpret this change by a subtraction of a constant component due to an axisymmet-

Table 8. Best 6-, 5- or 4-parameter fit of a quasi-periodic GP model obtained in our analysis of the stellar activity from the SPIRou B_ℓ data of the late-M dwarfs in our sample. The asterisk after a star name means that the measured period is more uncertain and has been obtained by a 4-parameter fit only.

Star	rotation period P_{rot} [d]	mean B_ℓ μ [G]	white noise σ [G]	amplitude α [G]	decay time l [d]	smoothing factor β	rms [G]	χ^2_{red}	visits
Priors	$\mathcal{U}(2, 300)$	$\mathcal{U}(-\infty, +\infty)$	$\mathcal{U}(0, +\infty)$	$\mathcal{U}(0, +\infty)$	$\mathcal{U}(50, 1000)$	$\mathcal{U}(0.25, 1.25)$			
GJ 1289	$74.0^{+1.5}_{-1.3}$	47^{+25}_{-25}	$2.4^{+2.5}_{-1.7}$	67^{+21}_{-12}	142^{+33}_{-26}	$0.64^{+0.17}_{-0.11}$	14.7	0.67	180
GJ 1103*	139^{+22}_{-23}	$8.2^{+10.1}_{-10.1}$	$4.1^{+4.0}_{-2.9}$	$18.2^{+8.9}_{-5.9}$			16.4	0.83	62
Gl 699*	$137.1^{+6.8}_{-4.0}$	$3.0^{+5.7}_{-5.8}$	$1.1^{+1.1}_{-0.8}$	$14.7^{+3.0}_{-2.4}$			8.7	0.77	243
Gl 15B*	$116.5^{+6.4}_{-4.7}$	$-0.3^{+6.3}_{-6.2}$	$2.1^{+2.1}_{-1.4}$	$13.8^{+3.8}_{-2.8}$			16.5	0.78	184
GJ 1151*	158^{+14}_{-9}	$-9.6^{+13.4}_{-13.2}$	$2.7^{+2.6}_{-1.9}$	$29.6^{+8.2}_{-5.5}$			15.7	0.83	153
Gl 905	$109.5^{+4.9}_{-5.4}$	-14^{+11}_{-11}	$1.7^{+1.8}_{-1.2}$	$29.4^{+8.1}_{-5.3}$	149^{+26}_{-25}	$0.71^{+0.21}_{-0.17}$	12.6	0.73	216
GJ 1286*	203^{+14}_{-21}	36^{+19}_{-20}	$5.7^{+4.5}_{-3.8}$	44^{+14}_{-10}			25.0	0.89	108
GJ 1002	$93.0^{+1.4}_{-1.7}$	$-6.4^{+12.5}_{-14.2}$	$4.1^{+3.4}_{-2.8}$	$20.4^{+9.7}_{-5.9}$		$0.90^{+0.24}_{-0.31}$	19.9	1.05	154

Table 9. Comparison of the rotation periods given in the literature with our measured values for the late Ms.

Reference	Category	GJ 1289	Gl 699	GJ 1151	Gl 905	GJ 1286	GJ 1002
This work	B_ℓ	74.0 ± 1.4					
Benedict et al. (1998)	phm		137 ± 5	158 ± 12	110 ± 5	203 ± 18	93.0 ± 1.6
Irwin et al. (2011)	phm		130.4				
Suárez Mascareño et al. (2015)	act		148.6 ± 0.1				
Moutou et al. (2017)	ZDI	54 ± 4					
Newton et al. (2018)	phm						88.92
Toledo-Padrón et al. (2019)	phm		145 ± 15				
Díez Alonso et al. (2019)	phm	83.6 ± 7.0		125 ± 23	106 ± 6		
Sabotta et al. (2021)	act		311.25		178.74		
Suárez Mascareño et al. (2022)	act						126 ± 15

ric magnetic field. This is the case of Gl 408, Gl 338B, Gl 436, GJ 4063 and Gl 617B. For other stars, the rate of detection does not significantly change when comparing the median-subtracted profiles to the original Stokes V profiles. This is the case of PM J21463+3813, Gl 412A, PM J08402+3127, Gl 480, GJ 1148 among the stars without a detected rotation period. We plan a more detailed study of the magnetic topology of the stars in our sample to further investigate the reasons of these non-detections.

5. Discussion and conclusions

In this paper, we have shown that spectropolarimetry is a useful technique for measuring the rotation period of a star, even for quiet M dwarfs. In our sample of 43 such stars, we could reliably measure the rotation period for 27, 8 of them being previously unknown. The rotation periods cover a large range in this sample of quiet stars, from 10 to 450 days. The agreement with other techniques, such as photometry or stellar activity indicators is good, except for a few stars (for instance Gl 251, Gl 411, Gl 846) where some techniques find a harmonic of the rotation period or converge toward very different values. The amplitude of variation of the longitudinal magnetic field for these quiet M dwarfs ranges from 3 G (Gl 338B, Gl 445) to 20 G for the major-

ity of the stars in our sample, but it can reach up to 70 G in some cases (GJ 1289) which is comparable to more active stars such as AD Leo (Gl 388: 45 ± 6 G, Carmona et al., in prep) or EV Lac (Gl 1873: 149 ± 17 G) over the same period of observations. The FWHM of the median Stokes I profile is another important measurement, as it may reveal a broadening due to the Zeeman effect for active stars. As the FWHM is sensitive to the total magnetic field (small and large-scale), while the longitudinal magnetic field is more sensitive to the large-scale field, a large amplitude of variation of the longitudinal field does not correlate necessarily with a large value of FWHM and both measures are therefore important. The average value over our sample is 6.07 km s^{-1} with a standard deviation of 0.66 km s^{-1} , clearly larger than the mean uncertainty of each FWHM in Table 1. This evidences a real dispersion among the mean FWHM values, which will be further investigated by using different line lists (low and high Landé factors) and by studying the time variation of the measured FWHM for a given star, as in Bellotti et al. (in prep) for AD Leo.

We divided our sample into 3 sub-categories according to the absolute magnitude in *Gaia G* band, roughly corresponding to early-, mid- and late-M dwarfs. There is a clear tendency to smaller values of the FWHM of the median Stokes I

Table 10. Best 4-parameter fit of a quasi-periodic GP model obtained in our analysis of the stellar activity from the SPIRou B_ℓ data of the M dwarfs in our sample without a clear periodic variation detection.

Star	mean B_ℓ μ [G]	white noise σ [G]	amplitude α [G]	rms [G]	χ^2_{red}	number of visits	rotation period from literature P_{rot} [d]	reference
Priors	$\mathcal{U}(-\infty, +\infty)$	$\mathcal{U}(0, +\infty)$	$\mathcal{U}(0, +\infty)$					
Gl 338B	$-8.1^{+1.6}_{-1.6}$	$1.3^{+1.0}_{-0.9}$	$3.1^{+1.6}_{-1.4}$	4.4	1.03	58	16.66	Sabotta et al. (2021)
Gl 617B	$19.3^{+4.0}_{-4.0}$	$1.4^{+1.5}_{-1.0}$	$8.9^{+2.9}_{-2.1}$	8.2	0.71	142		
Gl 412A	$13.7^{+4.1}_{-4.3}$	$4.0^{+1.2}_{-1.4}$	$10.7^{+3.5}_{-2.5}$	9.7	1.23	174	100.9 ± 0.3	Suárez Mascareño et al. (2018)
Gl 480	$6.6^{+3.5}_{-3.3}$	$5.5^{+1.8}_{-2.1}$	$6.9^{+2.8}_{-2.3}$	11.0	1.28	104		
Gl 436	$-10.4^{+2.2}_{-2.0}$	$1.6^{+1.6}_{-1.1}$	$4.4^{+2.1}_{-1.7}$	7.5	0.81	85	44.09 ± 0.08	Bourrier et al. (2018)
Gl 408	$-43.8^{+3.6}_{-3.6}$	$1.4^{+1.4}_{-1.0}$	$8.7^{+2.6}_{-2.0}$	9.1	0.79	168		
Gl 317	$-10.8^{+8.4}_{-8.8}$	$2.7^{+2.5}_{-1.9}$	$14.5^{+8.2}_{-4.1}$	11.9	0.97	76		
GJ 4063	$17.8^{+3.3}_{-3.2}$	$2.9^{+1.9}_{-1.9}$	$7.1^{+2.3}_{-1.8}$	11.4	0.96	204	40.2 ± 0.8	Díez Alonso et al. (2019)
GJ 1012	$6.4^{+2.6}_{-2.6}$	$3.2^{+2.7}_{-2.2}$	$4.0^{+3.8}_{-2.7}$	15.9	0.99	135		
GJ 1148	$-9.1^{+3.9}_{-3.5}$	$2.3^{+2.4}_{-1.6}$	$7.1^{+4.1}_{-2.9}$	13.9	0.81	101	71.5 ± 5.1	Díez Alonso et al. (2019)
PM J08402+3127	16^{+20}_{-21}	$4.6^{+3.8}_{-3.1}$	39^{+16}_{-9}	18.8	0.98	139	118 ± 14	Díez Alonso et al. (2019)
Gl 725B	$-4.6^{+5.2}_{-5.1}$	$1.2^{+1.3}_{-0.8}$	$12.1^{+3.7}_{-2.8}$	10.7	0.75	209		
GJ 1105	$1.2^{+3.6}_{-3.1}$	$2.4^{+2.2}_{-1.7}$	$7.3^{+3.2}_{-2.7}$	13.5	0.93	161		
Gl 445	$-1.8^{+2.7}_{-2.6}$	$3.4^{+3.2}_{-2.4}$	$3.2^{+3.7}_{-2.3}$	17.4	0.97	90		
PM J21463+3813	$-0.4^{+7.5}_{-7.7}$	$3.1^{+3.1}_{-2.2}$	$16.3^{+6.6}_{-4.6}$	20.7	0.84	176		
Gl 447	$20.5^{+9.1}_{-9.5}$	$4.8^{+3.0}_{-3.0}$	$16.6^{+8.5}_{-5.3}$	14.9	1.13	57	165.1 ± 0.8	Suárez Mascareño et al. (2016)

profile toward mid-type stars with averages and standard deviations for the 3 groups of 6.65 and 0.59 km s $^{-1}$ (early-type), 5.73 and 0.34 km s $^{-1}$ (mid-type), 6.49 and 0.75 km s $^{-1}$ (late-type), respectively. The larger dispersion in the early-type and late-type groups may be due to a few active outliers: removing Gl 410 from the early-type group gives new average and standard deviation of 6.45 and 0.40 km s $^{-1}$, respectively, while for the late-type group, removing GJ 1286 and GJ 1289 gives 6.14 and 0.52 km s $^{-1}$, respectively, now more compatible with the mid-type group, given the small size of the early- and late-type groups. The most extreme values correspond to Gl 411 (4.93 ± 0.18 km s $^{-1}$) and Gl 410 (7.73 ± 0.21 km s $^{-1}$). A test on GJ 1289 shows that the measured FWHM clearly depend on the minimum adopted depth (0.03 in this work), the LSD mask (3000 and 3500 K give different results for this 3238 K star), and does not clearly show an increase when using masks limited to low Landé factors ($g_{\text{eff}} \leq 1.2$) versus large Landé factors ($g_{\text{eff}} > 1.2$). The possible effect of the magnetic field on the Stokes I FWHM of the stars in this sample will be studied in detail in Donati et al. (in prep) and Cristofari et al. (in prep).

We observe that it is easier to constrain the rotation period and the other parameters of the GP for early-type stars, even if the amplitude of variation of the longitudinal magnetic field is similar in the other two sub-categories. This may be due to the fact that they are brighter in average than later M dwarfs. Additionally, the decay time seems well constrained between 50 and 100 days for the early-type stars. For the mid-M dwarfs, it lies around 100 days while for the late-M dwarfs, it seems to be larger at about 150 days, although these results are only based on 3 and 2 measurements, respectively. There is a tendency to have longer decay times for larger stellar rotation period. Clearly, the quasi-periodic GP fit converges more easily for the early-type stars than for the others: it converges for only 60% of the mid-type stars and, although the convergence rate is similar for the

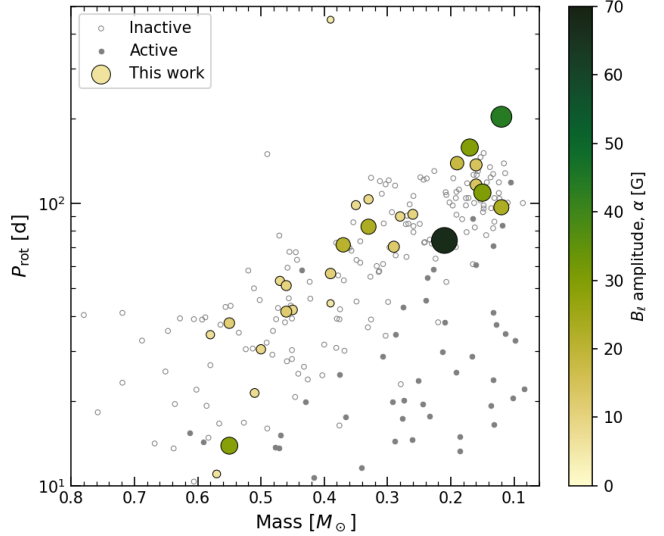


Fig. 11. Rotation period vs stellar mass diagram. Stars with rotation periods determined in this work are shown as larger circles, where the symbol sizes and colors are proportional to the amplitude of variation of B_ℓ (see α values given in Tables 3, 5, and 8). Rotation periods and mass determinations for inactive (white circles) and active (gray circles) stars from Newton et al. (2017) are shown for comparison.

late-type and the early-type stars, we have to use a 4-parameter fit for the late-type stars (fixing the smoothing factor and the decay time) while we can use a 6-parameter fit for the early-type stars with good constraints on the smoothing factor and on the decay time.

Our sample is too small to infer general properties of M stars. Therefore, we compare in Fig. 11 the sample of stars analyzed

in this paper to more complete non-magnetic studies in which active and inactive stars are well represented. We include a total of 212 M stars from Newton et al. (2017), whose mass and rotation periods are similar to the range explored in this paper. Our sample of quiet stars nicely fit the sequence of inactive stars as expected. The long rotation period of Gl 411 appears as an exception, and may in fact not reflect the stellar rotation period, as discussed in Sec. 4.2.

Low-mass stars arrive rapidly rotating on the main sequence and spin down with time as angular momentum is lost through magnetized winds (Barnes 2007). Empirically-calibrated relations between age and period can be used to estimate the ages of individual field stars. Gaidos et al. (2023) combined the 4 Gyr M-dwarf gyrochrone of the open cluster M 67 (Dungee et al. 2022) with those of younger, previously published gyrochrones (Curtis et al. 2020) to assign ages to M dwarf host stars with $T_{\text{eff}} = 3200\text{--}4200$ K. We use the same gyrochronology to estimate the ages of 20 stars in our sample with well measured rotation periods and T_{eff} in that range. Mean values and standard deviations are calculated from distributions constructed by 10000 Monte Carlo calculations incorporating uncertainties from P_{rot} (from Tables 5 and 8), the gyrochrones, T_{eff} (assumed ± 75 K), [Fe/H] (assumed to be ± 0.1 dex) and variation in the initial rotation periods of the stars on the zero-age main sequence. Results are given in Table 11: most stars are 4–10 Gyr old, with a few younger stars from 0.5 to 2 Gyr. The rotation-age relations are only valid for stars of approximately solar metallicity, but we give in the Table (col. 6) a correction computed using a theoretically-based model and the star metallicity, to be added to the age given in col. 4. We report age for members of binaries but emphasize that those stars could have distinct rotational histories due to tides and rapid dissipation of primordial disks (Fleming et al. 2019; Messina 2019).

The present study only exploits the longitudinal magnetic field measured from the spectropolarimetric data of the SPIRou SLS. Using the same data, much more can be done, for example investigating the magnetic topology of these stars and its evolution using ZDI maps.

Acknowledgements. Based on observations obtained at the Canada-France-Hawaii Telescope (CFHT) which is operated from the summit of Maunakea by the National Research Council of Canada, the Institut National des Sciences de l’Univers of the Centre National de la Recherche Scientifique of France, and the University of Hawaii. The observations at the Canada-France-Hawaii Telescope were performed with care and respect from the summit of Maunakea which is a significant cultural and historic site.

This work has made use of data from the European Space Agency (ESA) mission *Gaia* (<https://www.cosmos.esa.int/gaia>), processed by the *Gaia* Data Processing and Analysis Consortium (DPAC, <https://www.cosmos.esa.int/web/gaia/dpac/consortium>). Funding for the DPAC has been provided by national institutions, in particular, the institutions participating in the *Gaia* Multilateral Agreement.

This research has also made intensive use of the SIMBAD database and of the VizieR catalog access tool, operated at CDS, Strasbourg, France and of NASA’s Astrophysics Data System (ADS).

We made an extensive use of the DACE (Data Analysis Center for Exoplanets) software from the University of Geneva (Díaz et al. 2014; Delisle et al. 2016).

This work has made use of the VALD database, operated at Uppsala University, the Institute of Astronomy RAS in Moscow, and the University of Vienna.

X.D., A.C., P.C.Z., E.M. and S.B. and more generally most of the French authors of this paper acknowledge funding from the French National Research Agency (ANR) under contract number ANR18CE310019 (SPLaSH). This work is supported by the ANR in the framework of the *Investissements d’Avenir* program (ANR-15-IDEX-02), through the funding of the “Origin of Life” project of the Grenoble-Alpes University.

E.M. acknowledges funding from the *Fundação de Amparo à Pesquisa do Estado de Minas Gerais* (FAPEMIG) under the project number APQ-02493-22.

B.Z. acknowledges funding from the *Programa de Internacionalização da Coordenação de Aperfeiçoamento de Pessoal de Nível Superior* (CAPES-PrInt #88887.683070/2022-00) and FAPEMIG (APQ-01033-22).

J.-F.D. acknowledges funding from the European Research Council (ERC) under

the H2020 research & innovation programme (grant agreement #740651 New-Worlds).

N.J.C., E.A. and R.D. wish to thank the Natural Sciences and Engineering Research Council of Canada and the *Fonds Québécois de Recherche - Nature et Technologies*, the *Observatoire du Mont-Mégantic* and the Institute for Research on Exoplanets and acknowledge funding from *Développement Économique Canada, Québec’s Ministère de l’Éducation et de l’Innovation*, the Trottier Family Foundation and the Canadian Space Agency.

This research made use of the hosting service `github` and, among others, of the following software tools: `matplotlib` (Hunter 2007); `NumPy` (Harris et al. 2020); `SciPy` (Virtanen et al. 2020); `Astropy` (Astropy Collaboration et al. 2013, 2018); `emcee` (Foreman-Mackey et al. 2013); `corner` (Foreman-Mackey 2016); `george` (Ambikasaran et al. 2015); `barrycorpy` (Wright & Eastman 2014).

References

Aigrain, S., Hodgkin, S. T., Irwin, M. J., Lewis, J. R., & Roberts, S. J. 2015, MNRAS, 447, 2880

Ambikasaran, S., Foreman-Mackey, D., Greengard, L., Hogg, D. W., & O’Neil, M. 2015, IEEE Transactions on Pattern Analysis and Machine Intelligence, 38, 252

Angus, R., Morton, T., Aigrain, S., Foreman-Mackey, D., & Rajpaul, V. 2018, MNRAS, 474, 2094

Artigau, É., Astudillo-Defru, N., Delfosse, X., et al. 2014, in Society of Photo-Optical Instrumentation Engineers (SPIE) Conference Series, Vol. 9149, Proc. SPIE, 914905

Artigau, É., Cadieux, C., Cook, N. J., et al. 2022, AJ, 164, 84

Astropy Collaboration, Price-Whelan, A. M., Sipőcz, B. M., et al. 2018, AJ, 156, 123

Astropy Collaboration, Robitaille, T. P., Tollerud, E. J., et al. 2013, A&A, 558, A33

Babcock, H. W. 1947, ApJ, 105, 105

Bagnulo, S., Landolfi, M., Landstreet, J. D., et al. 2009, PASP, 121, 993

Bakos, G., Noyes, R. W., Kovács, G., et al. 2004, PASP, 116, 266

Barnes, S. A. 2007, ApJ, 669, 1167

Benedict, G. F., McArthur, B., Nelan, E., et al. 1998, AJ, 116, 429

Boisse, I., Bouchy, F., Hébrard, G., et al. 2011, A&A, 528, A4

Bonfils, X., Delfosse, X., Udry, S., et al. 2013, A&A, 549, A109

Bonfils, X., Mayor, M., Delfosse, X., et al. 2007, A&A, 474, 293

Bourrier, V., Lovis, C., Beust, H., et al. 2018, Nature, 553, 477

Burt, J., Vogt, S. S., Butler, R. P., et al. 2014, ApJ, 789, 114

Cook, N. J., Artigau, É., Doyon, R., et al. 2022, PASP, 134, 114509

Cortes-Zuleta, P., Boisse, I., Klein, B., et al. 2023, arXiv e-prints, arXiv:2301.10614

Cristofari, P. I., Donati, J. F., Masseron, T., et al. 2022, MNRAS, 516, 3802

Curtis, J. L., Agüeros, M. A., Matt, S. P., et al. 2020, ApJ, 904, 140

Delisle, J. B., Ségransan, D., Buchschacher, N., & Alesina, F. 2016, A&A, 590, A134

Díaz, R. F., Almenara, J. M., Santerne, A., et al. 2014, MNRAS, 441, 983

Díaz, R. F., Delfosse, X., Hobson, M. J., et al. 2019, A&A, 625, A17

Díez Alonso, E., Caballero, J. A., Montes, D., et al. 2019, A&A, 621, A126

Donati, J. F., Kouach, D., Moutou, C., et al. 2020, MNRAS, 498, 5684

Donati, J. F., Morin, J., Petit, P., et al. 2008, MNRAS, 390, 545

Donati, J. F., Semel, M., Carter, B. D., Rees, D. E., & Collier Cameron, A. 1997, MNRAS, 291, 658

Dungee, R., van Saders, J., Gaidos, E., et al. 2022, ApJ, 938, 118

Faria, J. P., Adibekyan, V., Amazo-Gómez, E. M., et al. 2020, A&A, 635, A13

Feiden, G. A., Skidmore, K., & Jao, W.-C. 2021, ApJ, 907, 53

Figueira, P., Santos, N. C., Bonfils, X., et al. 2010, in EAS Publications Series, Vol. 42, EAS Publications Series, ed. K. Goździewski, A. Niedzielski, & J. Schneider, 131–135

Fleming, D. P., Barnes, R., Davenport, J. R. A., & Luger, R. 2019, ApJ, 881, 88

Foreman-Mackey, D. 2016, The Journal of Open Source Software, 1, 24

Foreman-Mackey, D., Hogg, D. W., Lang, D., & Goodman, J. 2013, PASP, 125, 306

Gaia Collaboration, Brown, A. G. A., Vallenari, A., et al. 2021, A&A, 649, A1

Gaidos, E., Claytor, Z., Dungee, R., Ali, A., & Feiden, G. A. 2023, MNRAS[arXiv:2301.12109]

Giles, H. A. C., Collier Cameron, A., & Haywood, R. D. 2017, MNRAS, 472, 1618

Gustafsson, B., Edvardsson, B., Eriksson, K., et al. 2008, A&A, 486, 951

Harris, C. R., Millman, K. J., van der Walt, S. J., et al. 2020, Nature, 585, 357

Haywood, R. D., Collier Cameron, A., Queloz, D., et al. 2014, MNRAS, 443, 2517

Hébrard, É. M., Donati, J. F., Delfosse, X., et al. 2016, MNRAS, 461, 1465

Henry, G. W. 1999, PASP, 111, 845

Hobson, M. J., Bouchy, F., Cook, N. J., et al. 2021, A&A, 648, A48

Table 11. Gyrochronological ages of the stars in our sample. Errors on T_{eff} and [M/H] are assumed to be 75 K and 0.1 dex, respectively. The correction in the last column corresponds to the value to be added to the age due to the non-solar metallicity of the star.

Star	T_{eff} K	P_{rot} d	Age Gyr	[M/H] dex	Metallicity correction Gyr
Gl 846	3833	11.01 ± 0.20	< 0.53	0.07	0.1
Gl 410	3842	13.87 ± 0.08	0.89 ± 0.12	0.05	0.1
Gl 382	3644	21.32 ± 0.04	1.9 ± 0.6	0.15	0.2
Gl 514	3699	30.45 ± 0.14	3.8 ± 0.6	-0.07	-0.1
GJ 1289	3238	74.0 ± 1.4	3.8 ± 1.2	0.05	0.0
Gl 849	3502	41.4 ± 0.4	4.2 ± 1.0	0.35	0.4
Gl 205	3771	34.3 ± 0.4	5.2 ± 0.7	0.43	0.6
PM J09553-2715	3366	70.5 ± 3.8	5.2 ± 2.0	-0.03	-0.0
Gl 880	3702	37.7 ± 0.7	5.5 ± 0.8	0.26	0.4
Gl 169.1A	3307	91.9 ± 3.4	5.5 ± 2.4	0.13	0.1
Gl 687	3475	56.5 ± 0.9	5.9 ± 1.8	0.01	0.0
Gl 15A	3611	44.3 ± 0.2	6.0 ± 1.2	-0.33	-0.5
GJ 3378	3326	92.1 ± 4.7	6.0 ± 2.7	-0.05	-0.0
Gl 48	3529	51.2 ± 1.4	6.1 ± 1.6	0.08	0.1
Gl 15B	3272	116.5 ± 5.6	6.1 ± 3.0	-0.42	-0.2
Gl 876	3366	82.8 ± 1.4	6.2 ± 2.7	0.15	0.1
Gl 752A	3558	53.2 ± 4.2	7.1 ± 1.9	0.11	0.2
Gl 699	3311	137.1 ± 5.4	9.4 ± 5.0	-0.37	-0.2
Gl 251	3420	98.7 ± 8.2	10.8 ± 4.7	-0.01	-0.0
Gl 725A	3470	103.5 ± 4.8	14.8 ± 5.4	-0.26	-0.3

Horne, K. 1986, PASP, 98, 609

Howard, A. W., Marcy, G. W., Fischer, D. A., et al. 2014, ApJ, 794, 51

Huélamo, N., Figueira, P., Bonfils, X., et al. 2008, A&A, 489, L9

Hunter, J. D. 2007, Computing In Science & Engineering, 9, 90

Irwin, J., Berta, Z. K., Burke, C. J., et al. 2011, ApJ, 727, 56

Irwin, J., Charbonneau, D., Nutzman, P., & Falco, E. 2009, in Transiting Planets, ed. F. Pont, D. Sasselov, & M. J. Holman, Vol. 253, 37–43

Jao, W.-C., Henry, T. J., Gies, D. R., & Hambly, N. C. 2018, ApJ, 861, L11

Kane, S. R., Thirumalachari, B., Henry, G. W., et al. 2016, ApJ, 820, L5

Kanodia, S. & Wright, J. 2018, Research Notes of the AAS, 2, 4

Kiraga, M. & Stepien, K. 2007, Acta Astron., 57, 149

Lafarga, M., Ribas, I., Reiners, A., et al. 2021, arXiv e-prints, arXiv:2105.13467

Landi Degl'Innocenti, E. 1992, in Solar Observations: Techniques and Interpretation, ed. F. Sanchez, M. Collados, & M. Vazquez, 71

Landstreet, J. D. 1980, AJ, 85, 611

Landstreet, J. D. 1992, A&A Rev., 4, 35

Mann, A. W., Dupuy, T., Kraus, A. L., et al. 2019, ApJ, 871, 63

Martoli, E., Hébrard, G., Moutou, C., et al. 2020, A&A, 641, L1

Messina, S. 2019, A&A, 627, A97

Morin, J., Donati, J. F., Petit, P., et al. 2008, MNRAS, 390, 567

Morin, J., Donati, J. F., Petit, P., et al. 2010, MNRAS, 407, 2269

Moutou, C., Dalal, S., Donati, J. F., et al. 2020, A&A, 642, A72

Moutou, C., Hébrard, E. M., Morin, J., et al. 2017, MNRAS, 472, 4563

Nelson, B. E., Robertson, P. M., Payne, M. J., et al. 2016, MNRAS, 455, 2484

Newton, E. R., Irwin, J., Charbonneau, D., et al. 2017, ApJ, 834, 85

Newton, E. R., Mondrik, N., Irwin, J., Winters, J. G., & Charbonneau, D. 2018, AJ, 156, 217

Nicholson, B. A. & Aigrain, S. 2022, MNRAS, 515, 5251

Noyes, R. W., Weiss, N. O., & Vaughan, A. H. 1984, ApJ, 287, 769

Nutzman, P. & Charbonneau, D. 2008, PASP, 120, 317

Petit, P., Folsom, C. P., Donati, J. F., et al. 2021, A&A, 648, A55

Piskunov, N. E., Kupka, F., Ryabchikova, T. A., Weiss, W. W., & Jeffery, C. S. 1995, A&AS, 112, 525

Pojmanski, G. 1997, Acta Astron., 47, 467

Pollacco, D. L., Skillen, I., Collier Cameron, A., et al. 2006, PASP, 118, 1407

Preston, G. W. 1971, PASP, 83, 571

Queloz, D., Henry, G. W., Sivan, J. P., et al. 2001, A&A, 379, 279

Rasmussen, C. E. & Williams, C. K. I. 2006, Gaussian Processes for Machine Learning (MIT Press)

Rees, D. E. & Semel, M. D. 1979, A&A, 74, 1

Reinhold, T. & Hekker, S. 2020, A&A, 635, A43

Rivera, E. J., Lissauer, J. J., Butler, R. P., et al. 2005, ApJ, 634, 625

Robertson, P. & Mahadevan, S. 2014, ApJ, 793, L24

Robertson, P., Mahadevan, S., Endl, M., & Roy, A. 2014, Science, 345, 440

Ryabchikova, T., Piskunov, N., Kurucz, R. L., et al. 2015, Phys. Scr, 90, 054005

Sabotta, S., Schlecker, M., Chaturvedi, P., et al. 2021, A&A, 653, A114

Stock, S., Nagel, E., Kemmer, J., et al. 2020, A&A, 643, A112

Suárez Mascareño, A., González-Álvarez, E., Zapatero Osorio, M. R., et al. 2022, arXiv e-prints, arXiv:2212.07332

Suárez Mascareño, A., Rebolo, R., & González Hernández, J. I. 2016, A&A, 595, A12

Suárez Mascareño, A., Rebolo, R., González Hernández, J. I., & Esposito, M. 2015, MNRAS, 452, 2745

Suárez Mascareño, A., Rebolo, R., González Hernández, J. I., & Esposito, M. 2017, MNRAS, 468, 4772

Suárez Mascareño, A., Rebolo, R., González Hernández, J. I., et al. 2018, A&A, 612, A89

Toledo-Padrón, B., González Hernández, J. I., Rodríguez-López, C., et al. 2019, MNRAS, 488, 5145

Virtanen, P., Gommers, R., Oliphant, T. E., et al. 2020, Nature Methods, 17, 261

West, A. A., Hawley, S. L., Bochanski, J. J., et al. 2008, AJ, 135, 785

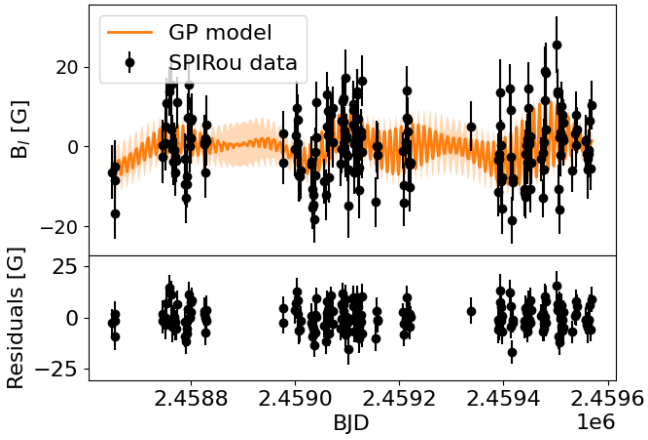
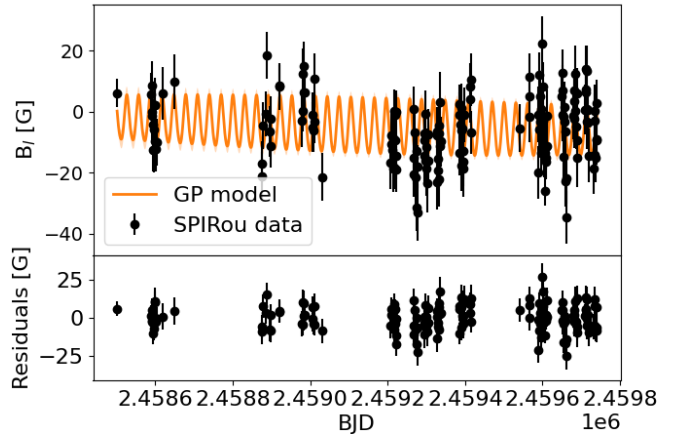
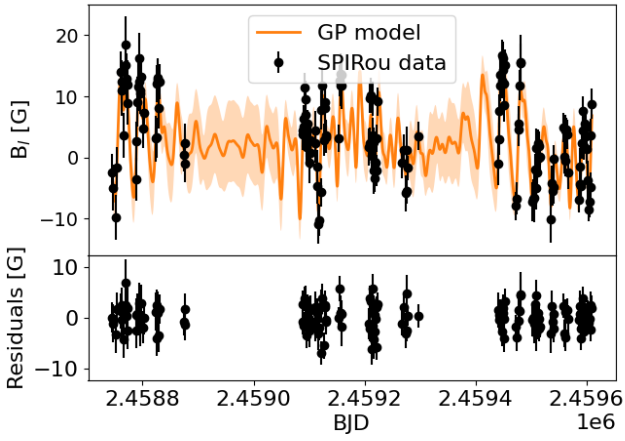
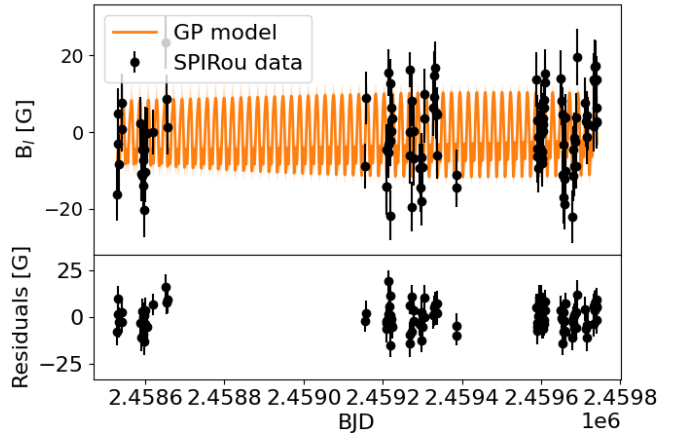
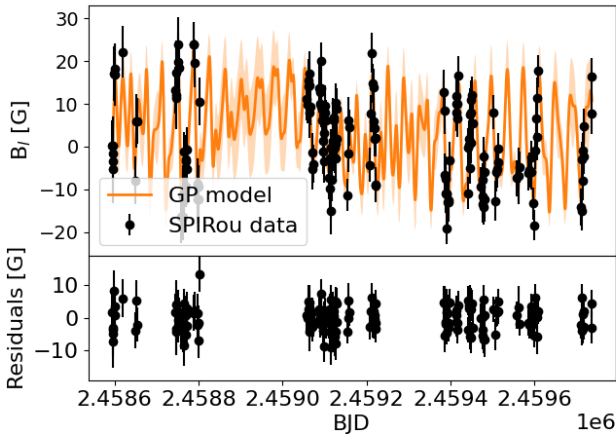
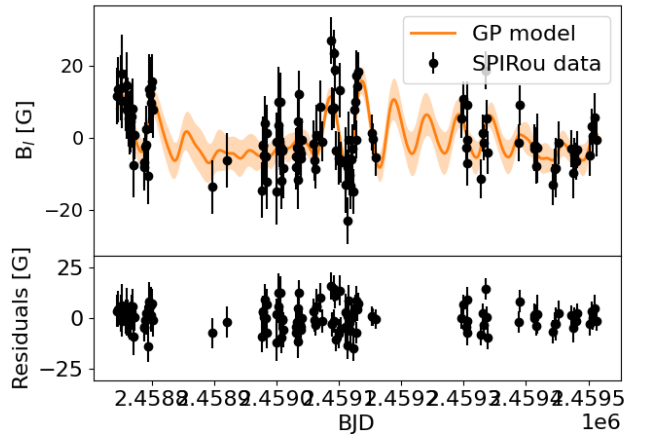
Woźniak, P. R., Vestrand, W. T., Akerlof, C. W., et al. 2004, AJ, 127, 2436

Wright, J. T. & Eastman, J. D. 2014, PASP, 126, 838

Zechmeister, M. & Kürster, M. 2009, A&A, 496, 577

Appendix A: Quasi-periodic Gaussian process regression for stars with a measured rotation period

We display here the temporal evolution of the longitudinal magnetic field and its GP fit leading to the measurement of the stellar rotation period for 25 stars of our sample (Figs. A.1 to A.24). The top panels of each Figure show the observed B_ℓ data (black points) and the orange line shows the best-fit quasi-periodic GP model. The bottom panels show the residuals. GP fits are generally 6-parameter fits, except when stated in the caption.

**Fig. A.1.** GP analysis of the SPIRou B_t data of Gl 846.**Fig. A.4.** Same for Gl 514.**Fig. A.2.** Same for Gl 205.**Fig. A.5.** Same for Gl 382.**Fig. A.3.** Same for Gl 880.**Fig. A.6.** Same for Gl 752A.

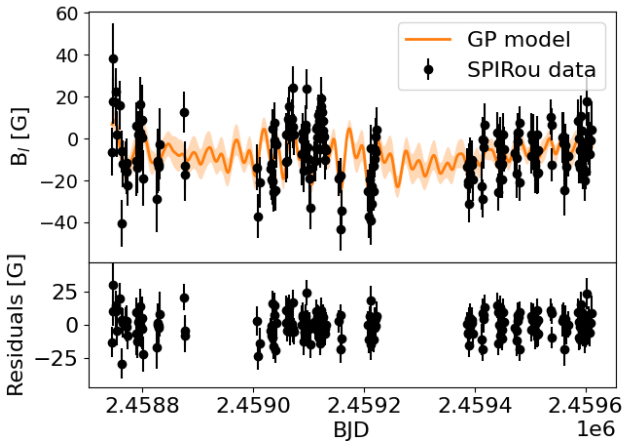


Fig. A.7. Same for Gl 48.

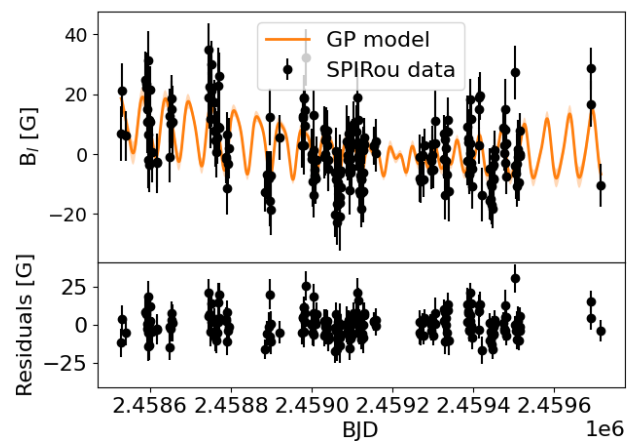


Fig. A.10. Same for Gl 687.

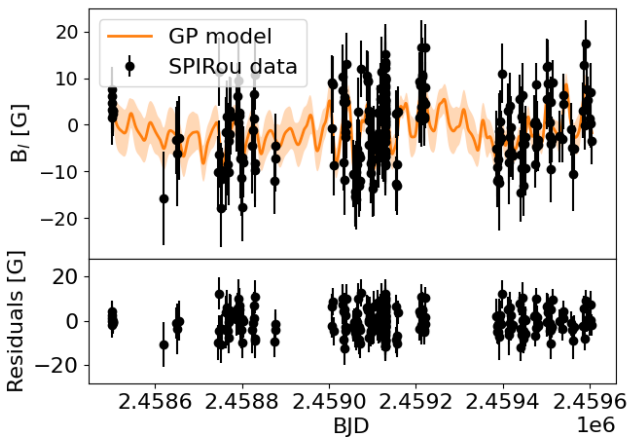


Fig. A.8. Same for Gl 15A.

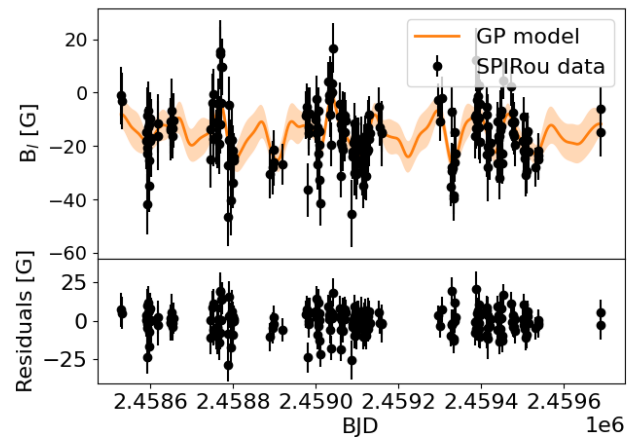


Fig. A.11. Same for Gl 725A (5-parameter fit).

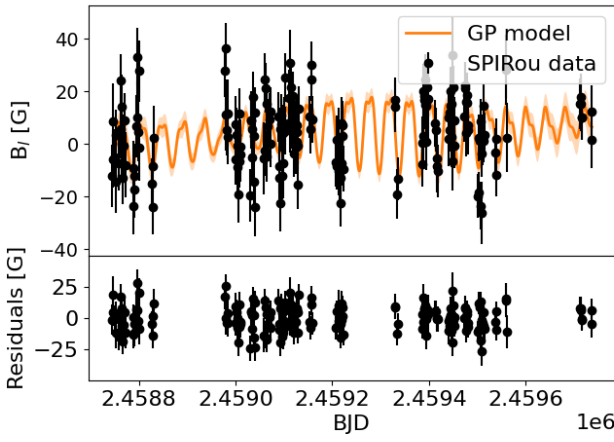


Fig. A.9. Same for Gl 849.

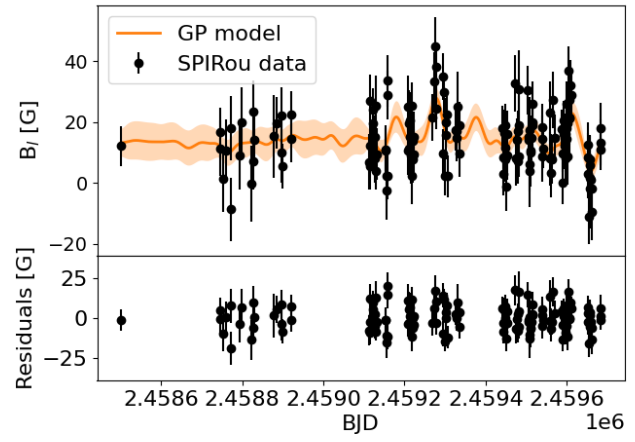
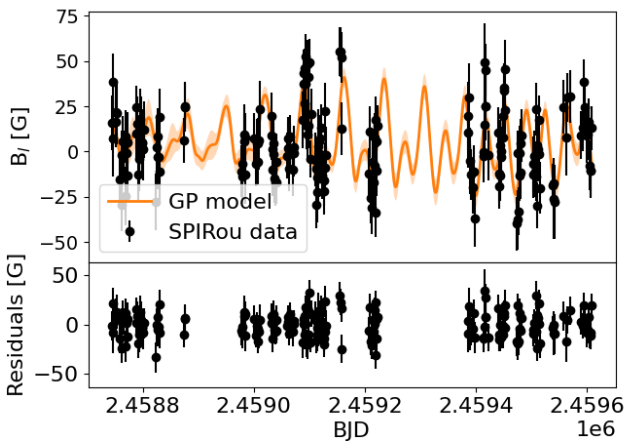
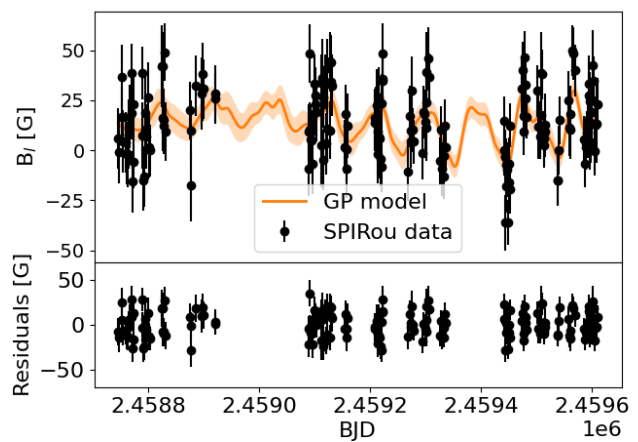
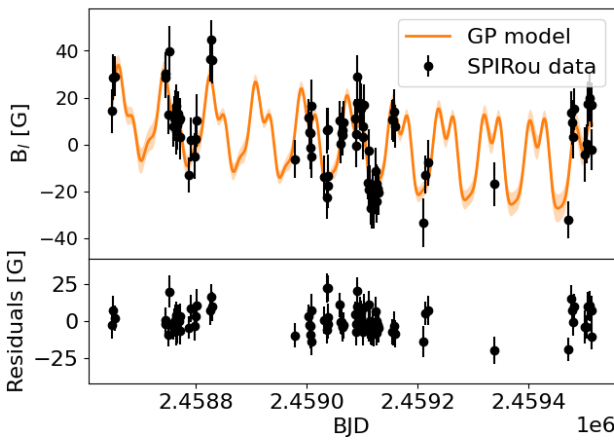
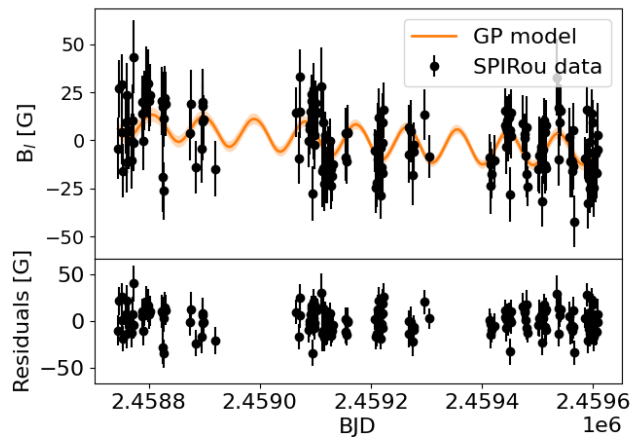
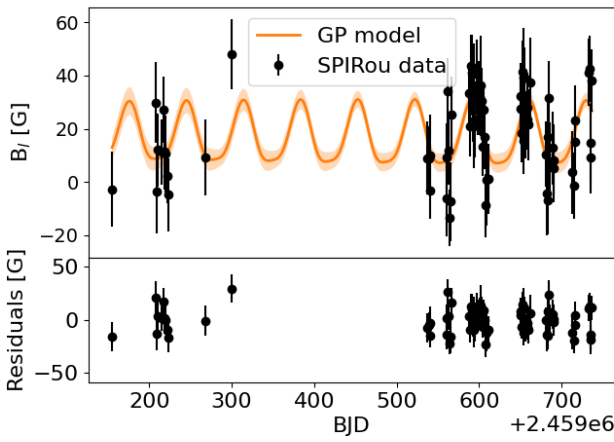
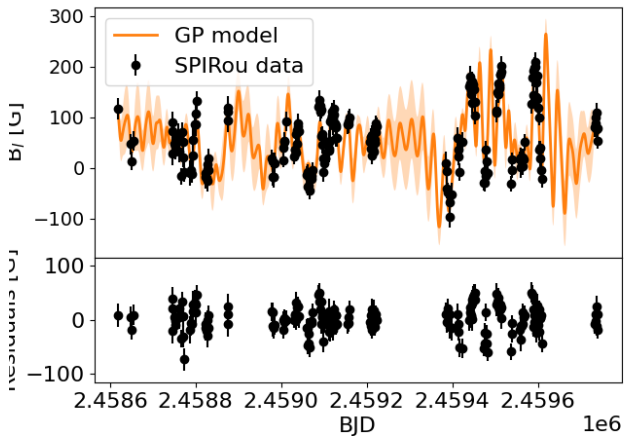


Fig. A.12. Same for Gl 251 (5-parameter fit).

**Fig. A.13.** Same for GJ 4333.**Fig. A.16.** Same for GJ 3378.**Fig. A.14.** Same for Gl 876.**Fig. A.17.** Same for Gl 169.1A.**Fig. A.15.** Same for PM J09553-2715.**Fig. A.18.** Same for GJ 1289.

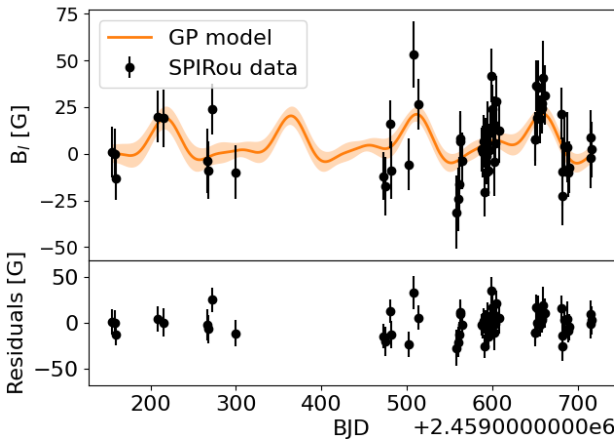


Fig. A.19. Same for GJ 1103 (5-parameter fit).

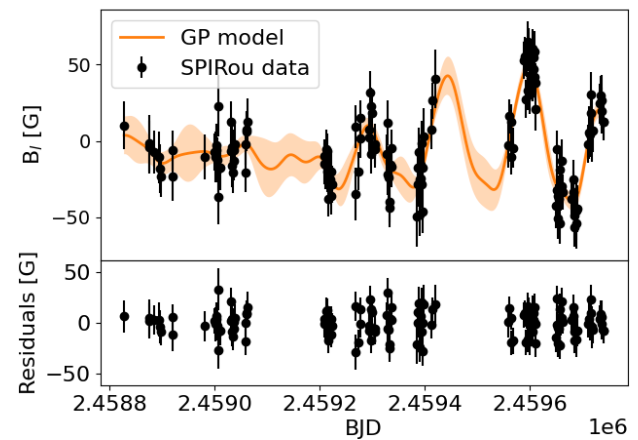


Fig. A.22. Same for GJ 1151 (5-parameter fit).

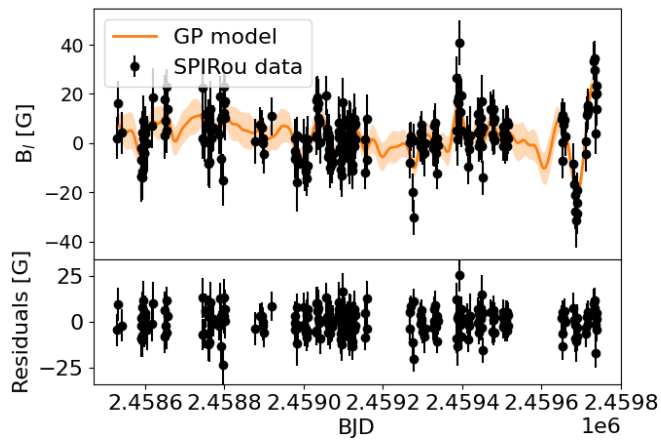


Fig. A.20. Same for Gl 699 (5-parameter fit).

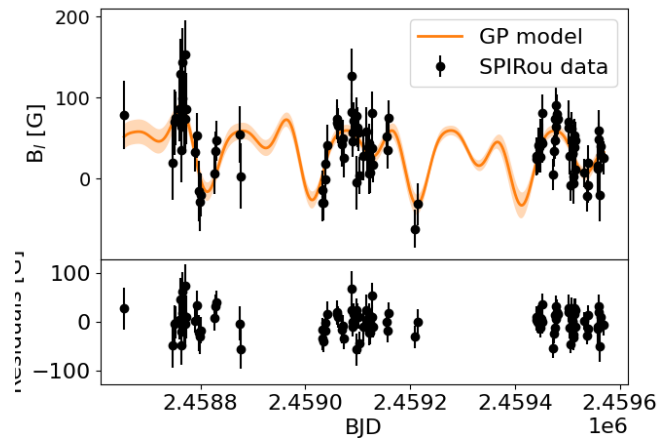


Fig. A.23. Same for GJ 1286 (5-parameter fit).

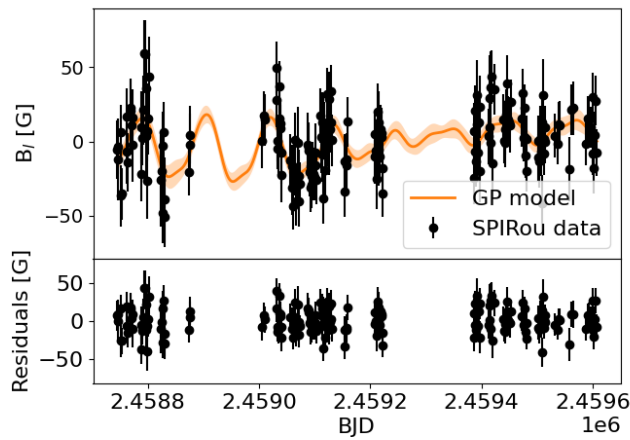


Fig. A.21. Same for Gl 15B (5-parameter fit).

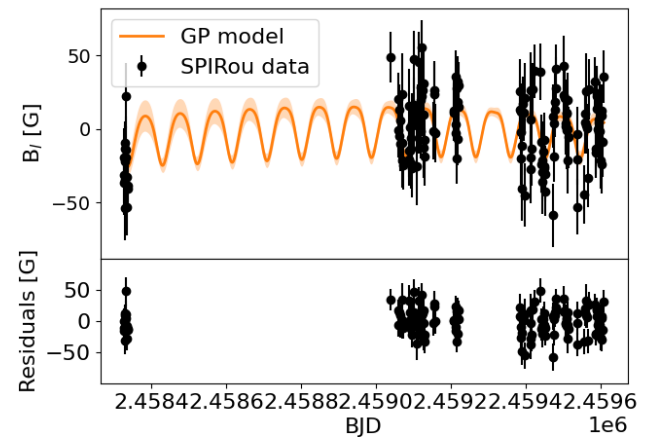


Fig. A.24. Same for GJ 1002.

Appendix B: Quasi-periodic Gaussian process regression for Gl 411

In this Appendix we study the particular case of the very long stellar rotation period measured for Gl 411 (460 days). We display the temporal evolution of the longitudinal magnetic field and its GP fit (Fig. B.1). The top panel shows the observed B_ℓ data (black points) and the orange line shows the best-fit quasi-periodic GP model. The bottom panel show the residuals of the 6-parameter GP fit. We then display the associated corner plot showing the posterior distributions of each parameter (Fig. B.3).

At the suggestion of the referee, we compare the GP fit to a similar GP fit to reshuffled data. We kept the same dates of observations, but attributed the B_ℓ measurements and their associated uncertainty randomly to a given date. The GP fit is now flat and shows that the detected periodicity in the actually measured data is real (Fig. B.2). We also display the associated corner plot for comparison where clearly no periodic behaviour can be detected (Fig. B.4).

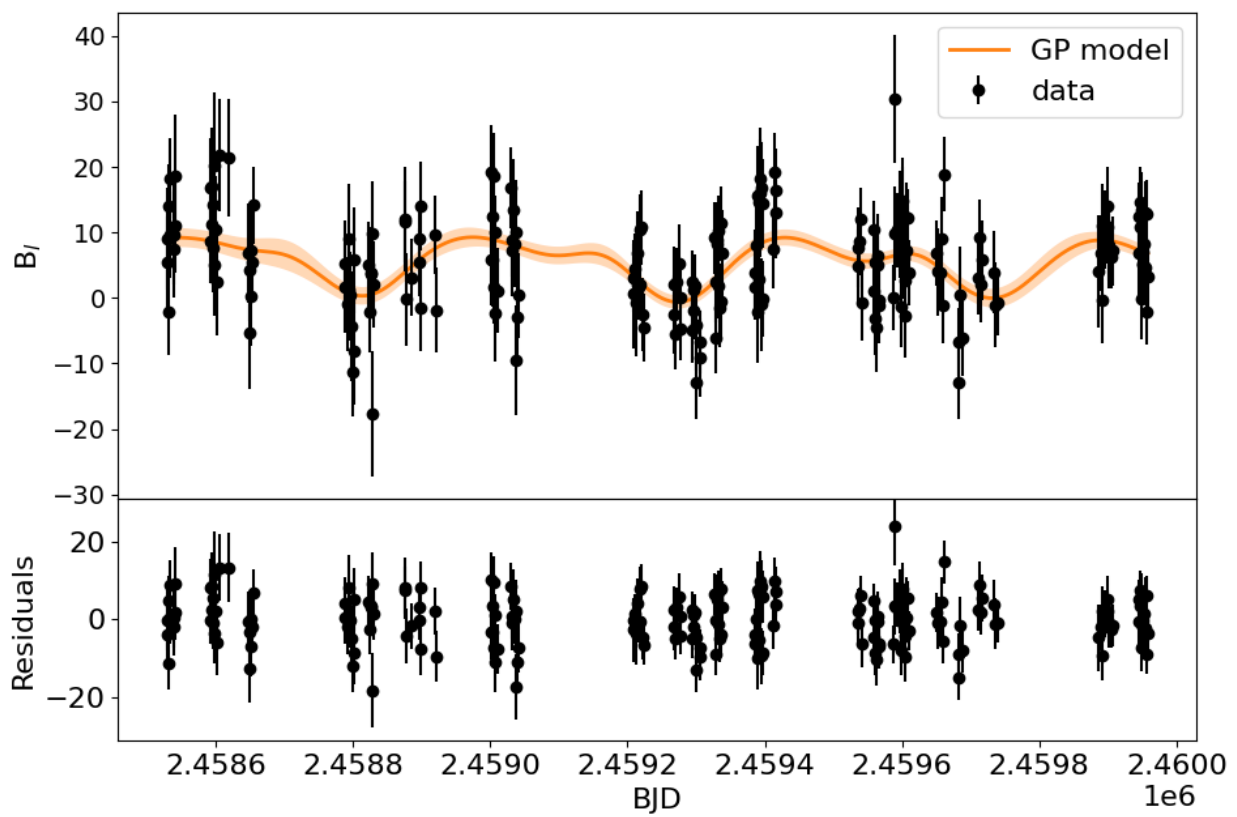


Fig. B.1. GP analysis of the SPIRou B_ℓ data of Gl411.

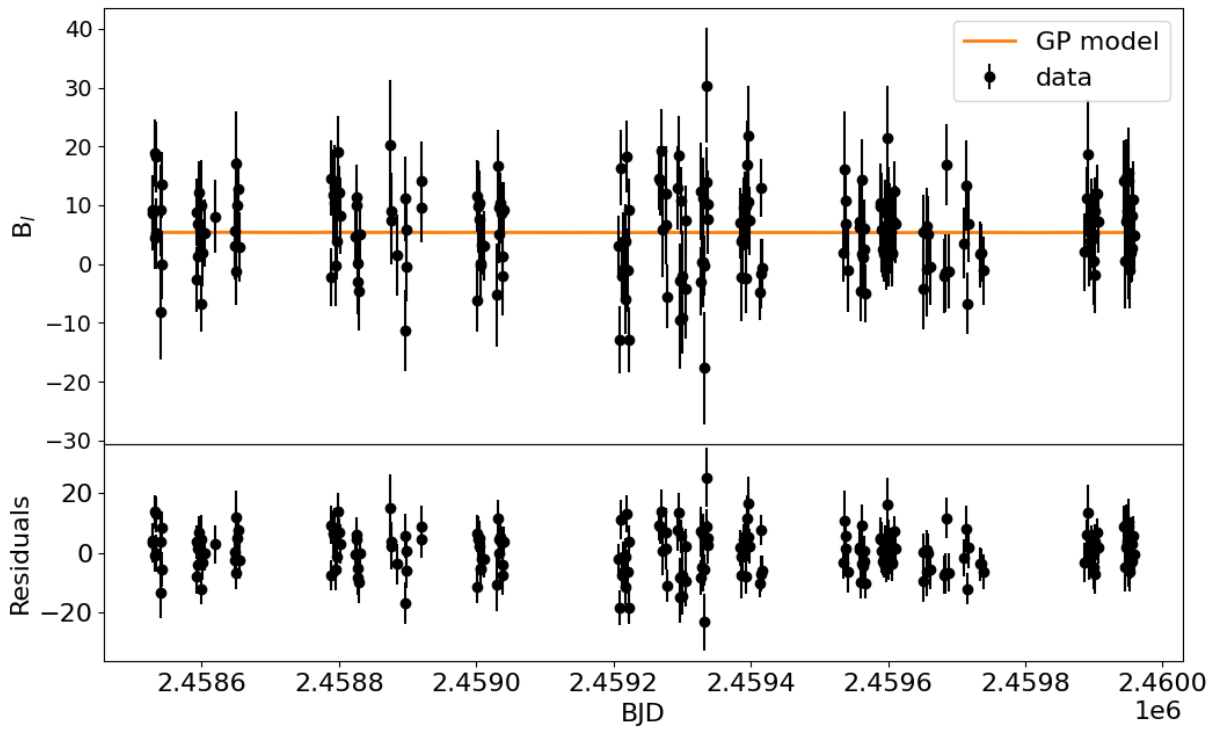


Fig. B.2. GP analysis of reshuffled B_t data at the same observation dates of Gl 411.

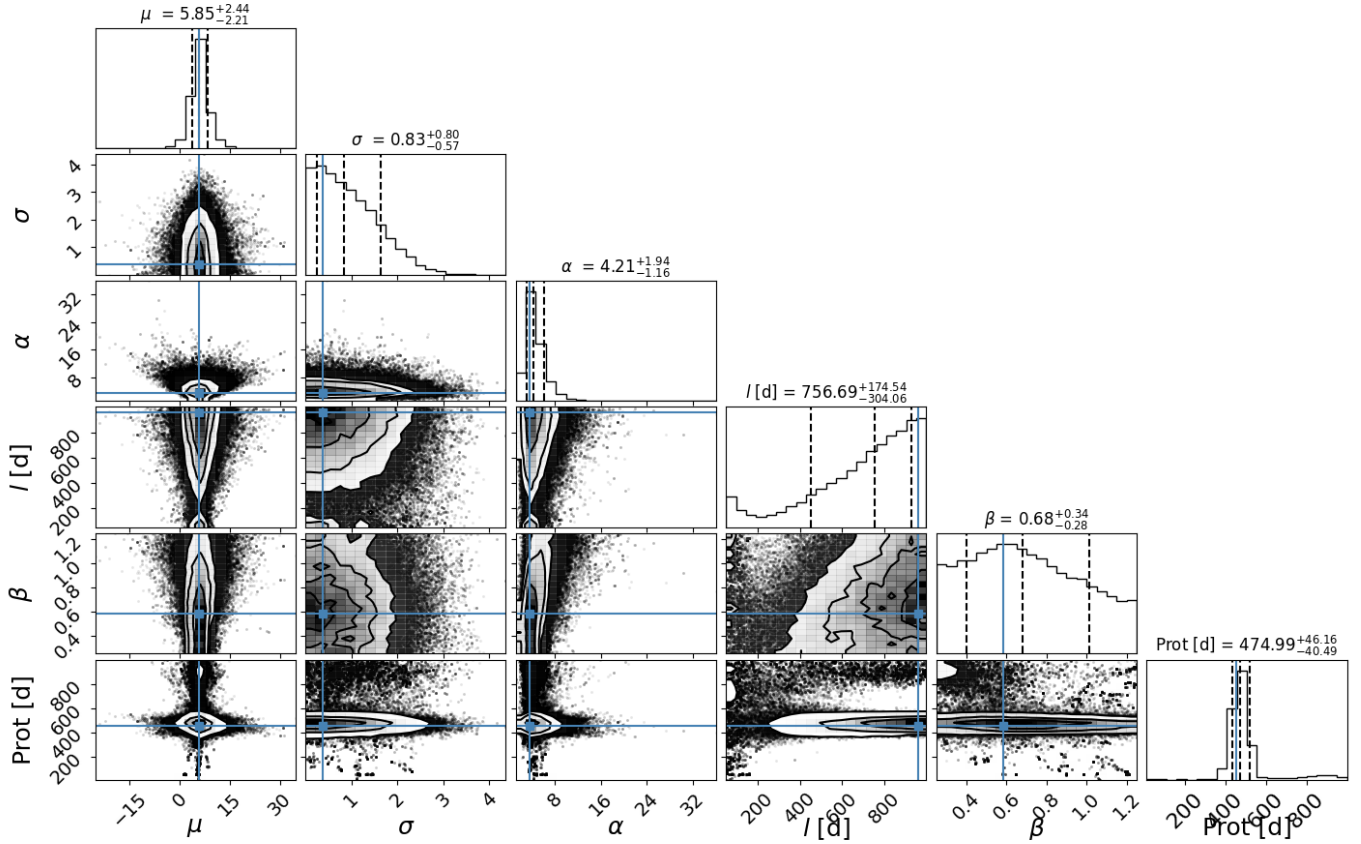


Fig. B.3. Corner plot of the posterior distribution of parameters of the GP fit for Gl 411.

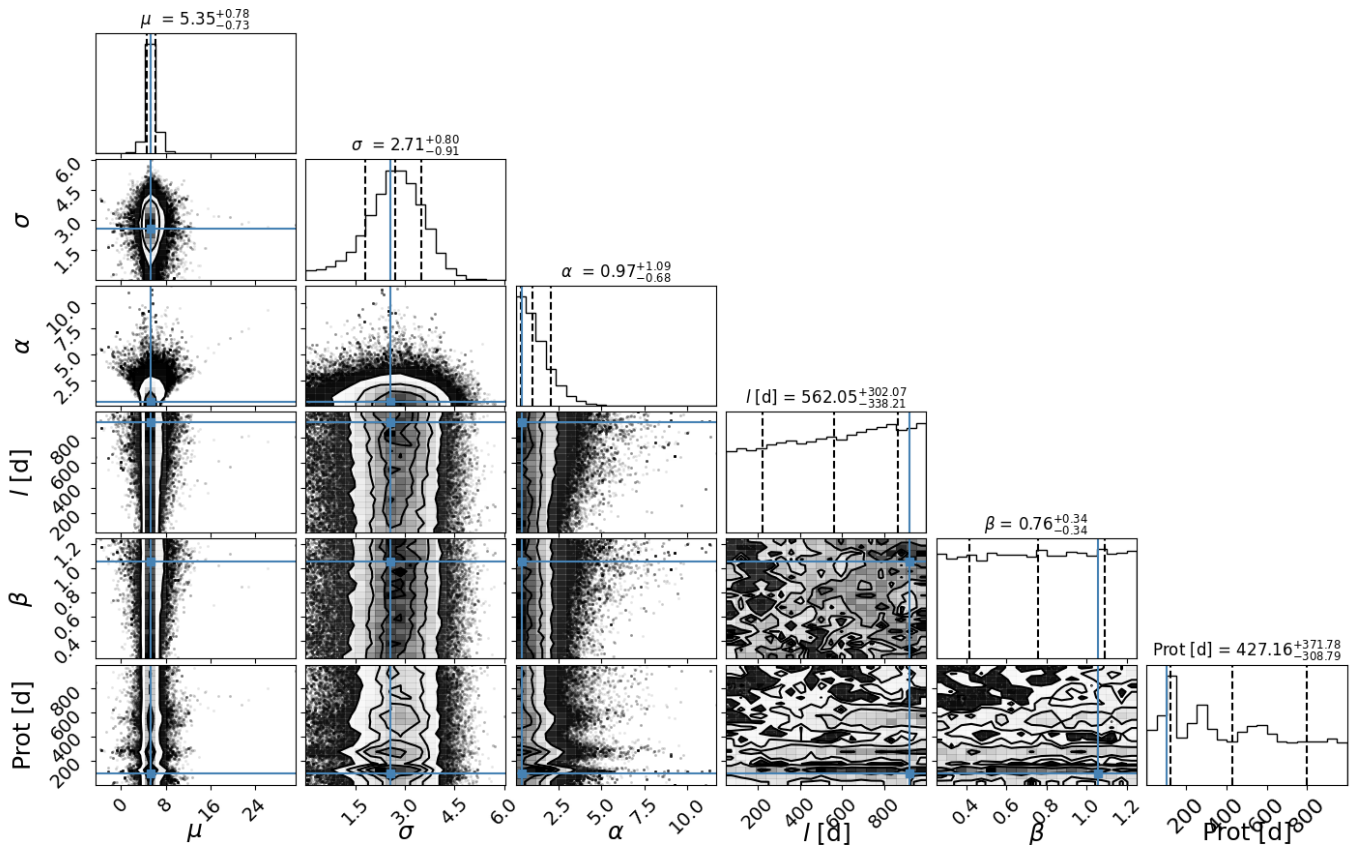


Fig. B.4. Corner plot of the posterior distribution of parameters of the GP fit for the reshuffled data at the observation dates of Gl 411.

Appendix C: Stokes V profiles of stars without a detection of rotation period

We display here the temporal evolution of the Stokes V for the 16 stars of our sample (Figs. C.1 to C.16) for which we could not detect a periodic variation of the longitudinal magnetic field. This shows that for some stars the Stokes V is well detected but constant or not varying periodically, while for others it is barely or not detected.

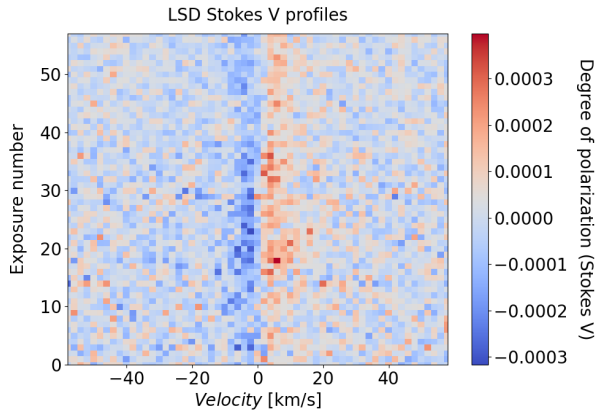


Fig. C.1. Temporal variation of the Stokes V profiles of the SPIRou polarimetric series of Gl 338B.

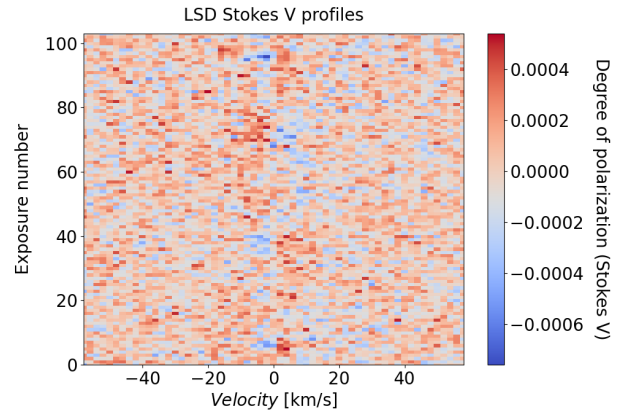


Fig. C.4. Same for Gl 480.

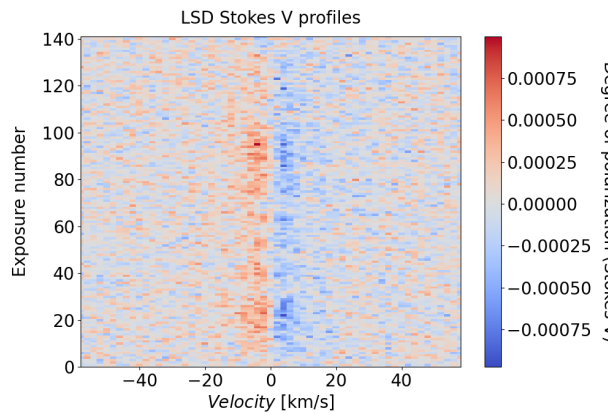


Fig. C.2. Same for Gl 617B.

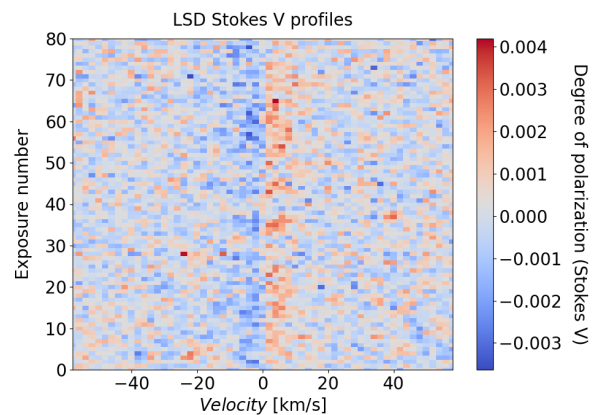


Fig. C.5. Same for Gl 436.

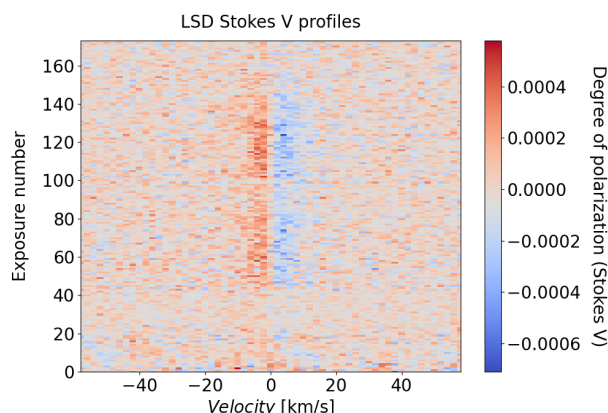


Fig. C.3. Same for Gl 412A.

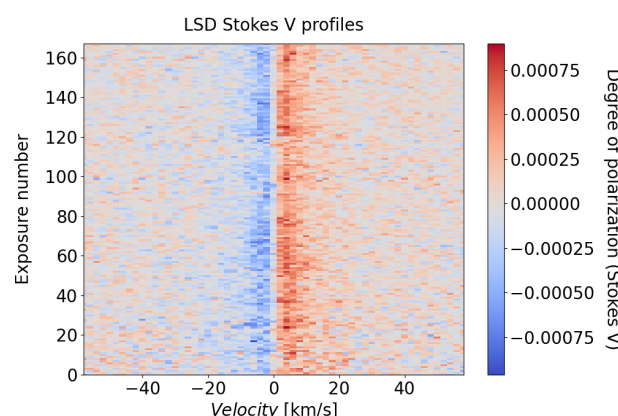
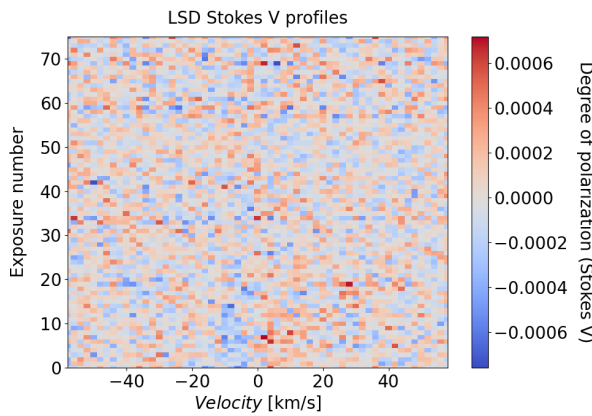
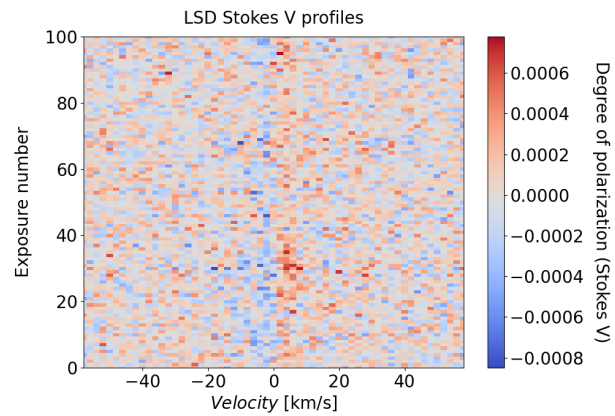
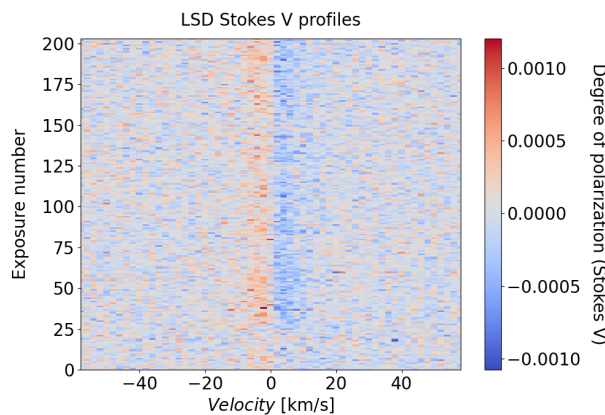
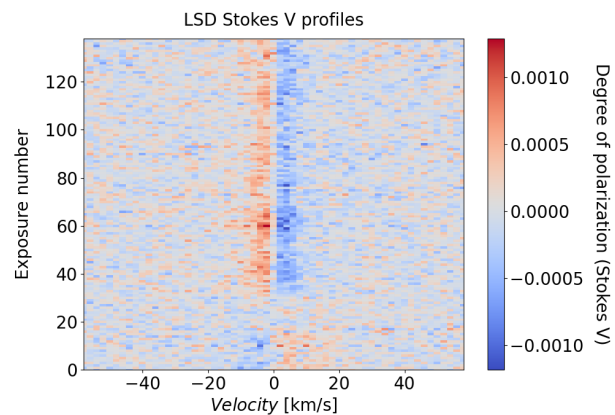
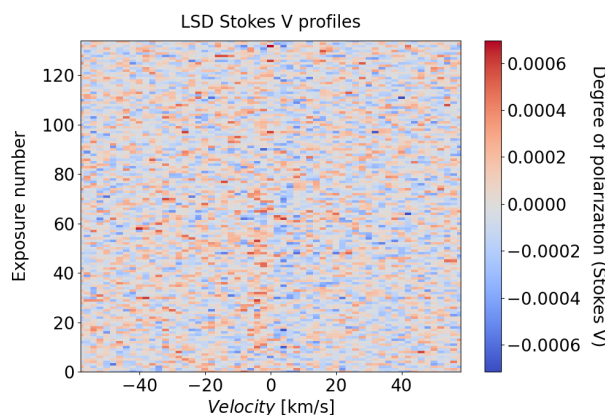
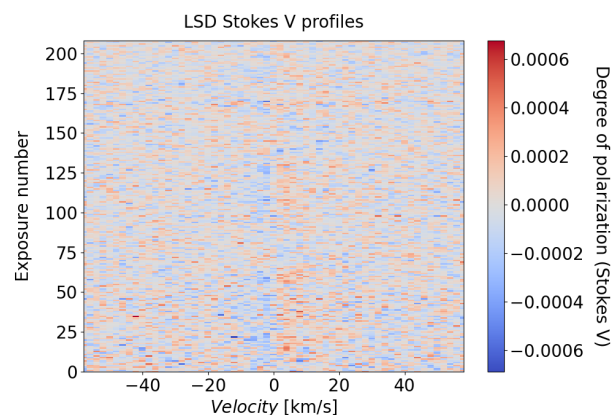


Fig. C.6. Same for Gl 408.

**Fig. C.7.** Same for Gl 317.**Fig. C.10.** Same for GJ 1148.**Fig. C.8.** Same for GJ 4063.**Fig. C.11.** Same for PM J08402+3127.**Fig. C.9.** Same for GJ 1012.**Fig. C.12.** Same for Gl 725B.

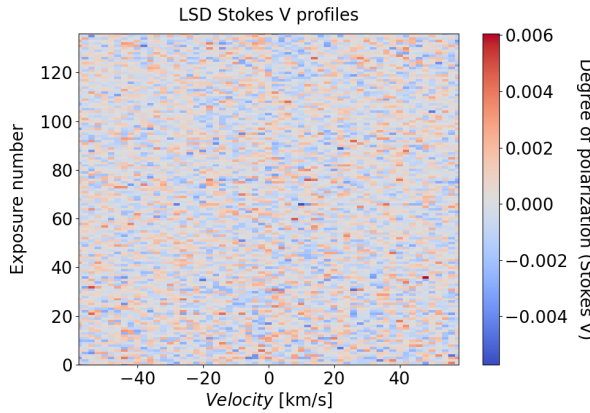


Fig. C.13. Same for GJ 1105.

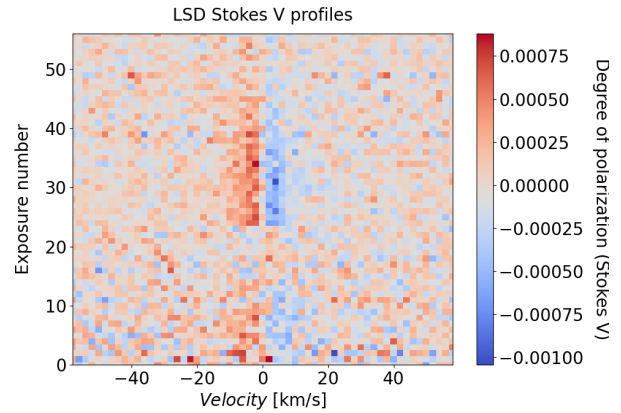


Fig. C.16. Same for Gl 447.

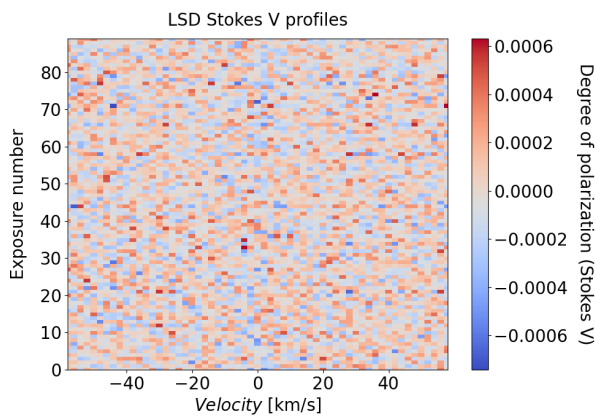


Fig. C.14. Same for Gl 445.

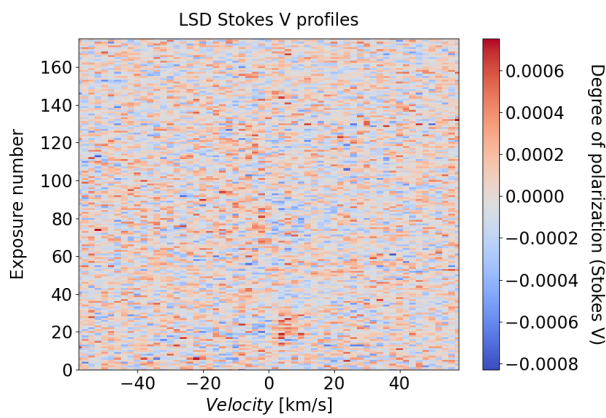


Fig. C.15. Same for PM J21463+3813.